UNIVERSITÀ DEGLI STUDI DI PADOVA

Dipartimento di Geoscienze

Direttore Prof. Cristina Stefani

Tesi di Laurea MAGISTRALE in GEOLOGIA E GEOLOGIA TECNICA

GEOLOGICAL MAPPING AND MULTISCALAR FRACTURE ANALYSIS OF SOME TEPUIS OF THE GRAN SABANA (VENEZUELA) BY USING REMOTE SENSING TECHNIQUES

Relatore: *Prof. Dario Zampieri*

Correlatori: Prof. Matteo Massironi

Prof. Francesco Sauro

Laureando: Riccardo Inama

ANNO ACCADEMICO 2015 / 2016

Contents

Abstract

The Gran Sabana Region (Venezuela) is characterized by the presence of some of the most impressive mountain in the world, called Tepuis. These unique flat-top mountains are carved in the Mataui Formation, a massive quartzitic sandstone representing the youngest deposit of the Proterozoic Roraima Group. This formation has been intruded by Proterozoic and Mesozoic Diabase dikes and sills, associated to hydrothermal alteration, which strongly affects the morphology of the Tepuis. In the first part of this work the various lithologies have been mapped using some advanced remote sensing techniques, resulting in a 1:25 000 geological map of the studied area.

The study area is deformed by large amplitude folds with WNW/ESE and NNE/SSW axis. In addition, the Tepuis are affected by a network of high-angle fractures. The analysis of the fracture systems on the Auyan and Chimantà tepuis reveals the existence of four main joint sets, the most prominent of which has N 30° direction, while two sets of conjugate joints are are arranged simmetrically to the main set. These fractures are interpreted in relation to the folding event with NNE/SSW axis. Accordingly, a main compressive stress oriented NW/SE has been inferred.

At the meso-scale additional fracture systems have been found analyzing a point cloud of a rock wall belonging to the Auyan Tepui. The comparison of structural data collected in the same area at the local and regional scales shows that the orientation of these groups of fracture planes does not match with the two sets found on the Auyan Tepui surface.

Introduction

This post-graduate thesis work, realized under the supervision of professors Dario Zampieri and Matteo Massironi, has been developed with the external contribute of prof. Francesco Sauro, geologist and speleologist. F. Sauro, after a PhD and several years of researches mostly based on tepuis cave exploration has acquired a deep knowledge on many aspects of these spectacular table mountains rising from the rainforest in the Gran Sabana of Venezuela. The idea of a multi disciplinary study, involving both structural and multispectral analyses, comes from the need of an overall view of all those geologic features that made and shaped this particular landscape. Although tepuis arouse interest in a broad spectrum of discipline (biology, ecology etc.), there is a lack in the geological bibliography; some studies have been carried out by Briceno et al. in the early nineties, but the latest available are specifically focused on speleology, with important references to geochemistry, water chemistry and mechanism of cave genesis. We aim to provide a more complete set of information, from a different point of view, which can be also used as a base for more specific studies (i.e. fieldwork) and will contribute to a better understanding of these quartz - arenitic table mountains.

Specifically, the work has been done by using some advanced remote sensing techniques, which consist in processing and analyzing various satellite images of Chimantà Massif and Auyan tepui, located in region of Gran Sabana, Venezuela. Image files have been downloaded for free from archives of ESA and NASA; both the space agencies provide on their websites a wide dataset of images collected by different satellites. In this case we opted for Landsat 8, Aster and the very recent Sentinel 2 files. Most of the subsequent elaborations were developed by means of ENVI and GIS software.

In particular, the first part of this experience consists in multispectral analysis and interpretation of the images named above. The different behavior of rocks in their

interaction with electro-magnetic radiation, is exploited by the software ENVI, with which is possible to analyze files using different combination of spectral bands. This makes us able to discriminate the different lithologies of the area, and draw a geological map. The second part of the work involves a structural study at the regional scale, which aims to look over the particular fracture network that characterize the outcrops; firstly, several different tectonic features have been identified, compared and ranked; then, we tried to link them to a suitable origin and reconstruct the tectonic history.

1. Geological setting

1.1 Geographic Overview

The studied area is located in the Gran Sabana region, part of the Guyana Shield. It extends over a wide surface, mostly in SE Venezuela, and spreads further over the borders with Brazil and Guyana, in the northern South America. The Guyana highland is also part of the "Upper Orinoco river basin" and is crossed by several tributaries of this river, the main of which is known as Caronì. The most impressive feature of Gran Sabana are the table top mountains (plateau, mesas and buttes) cropping out over the surrounding areas and rising above the savannah, with an elevation ranging from 1000 up to 3000 m a.s.l.. These particularly-shaped plateau are also named "Tepui", word that in the local Pemon language means "mountain".

Figure 1. Location of 1) Auyan Tepui and 2) Chimantà Massif in the Gran Sabana Region. In the box is shown the position of the area relatively to the northern part of South America. It is also possible to see the Caroni river on the left side. Images downloaded from Google maps and Google Earth.

Among the many tepuis of the Guyana Shield, we focused our research on two of them: Auyan Tepui (700 km^2), famous for the highest waterfall in the world (Salto Angel, with a vertical drop of about 975 m) and Chimantà Massif, which includes more different table mountains, with a total surface of 1470 Km^2 (Sauro, 2014).
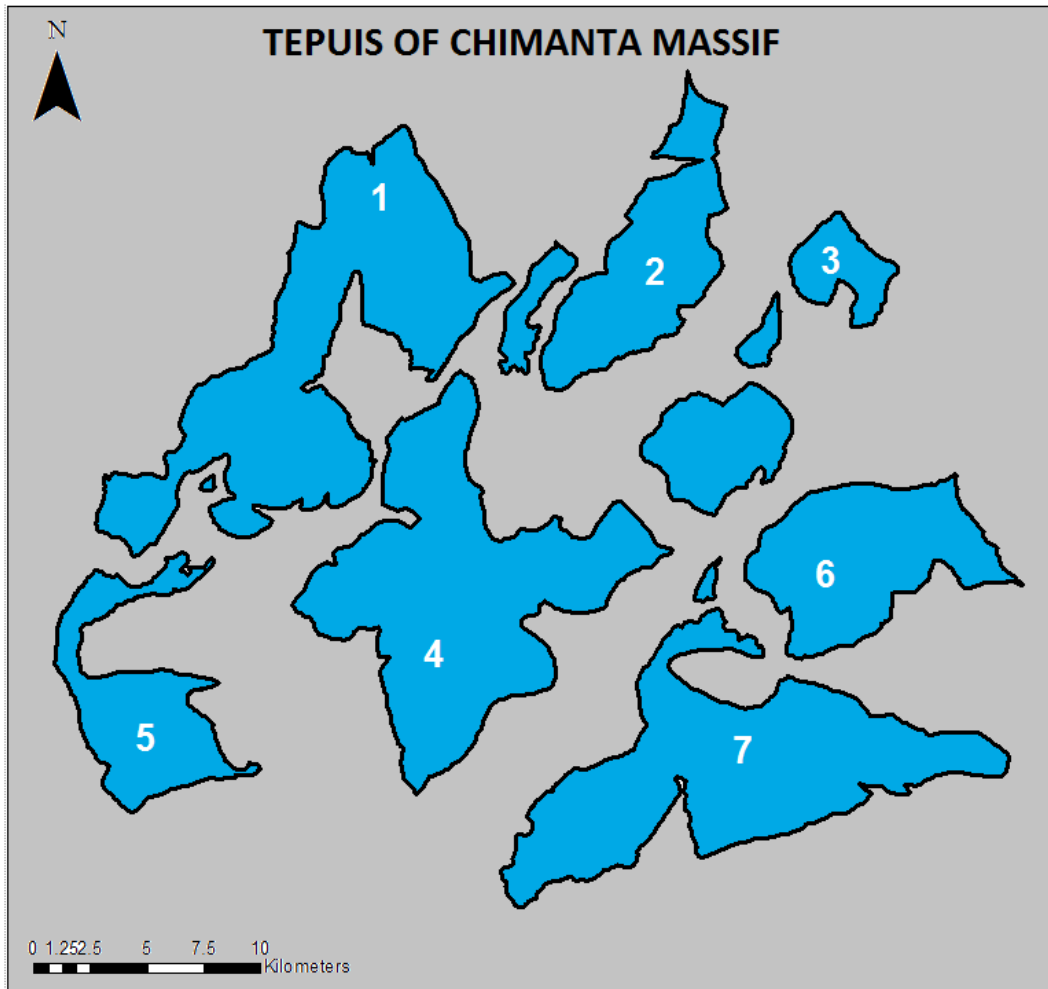
Figure 2. Sketch of the position of the main tepuis of the Chimantà Massif: -1) Apacarà ; -2) Euruoda; -3) Tirepon; -4) Toronò: -5) Abacapa; -6) Churi; -7) Acopan.

1.2 The Guyana Shield

The Guyana shield represents the northern part of the Amazon craton, which also includes the Brazilian shield in the central/southern part; this constitutes the older, Precambrian nucleus of South America (Briceno et. al. 1990). It has been subdivided into four geological provinces (Gonzales de Juana et al. 1980):
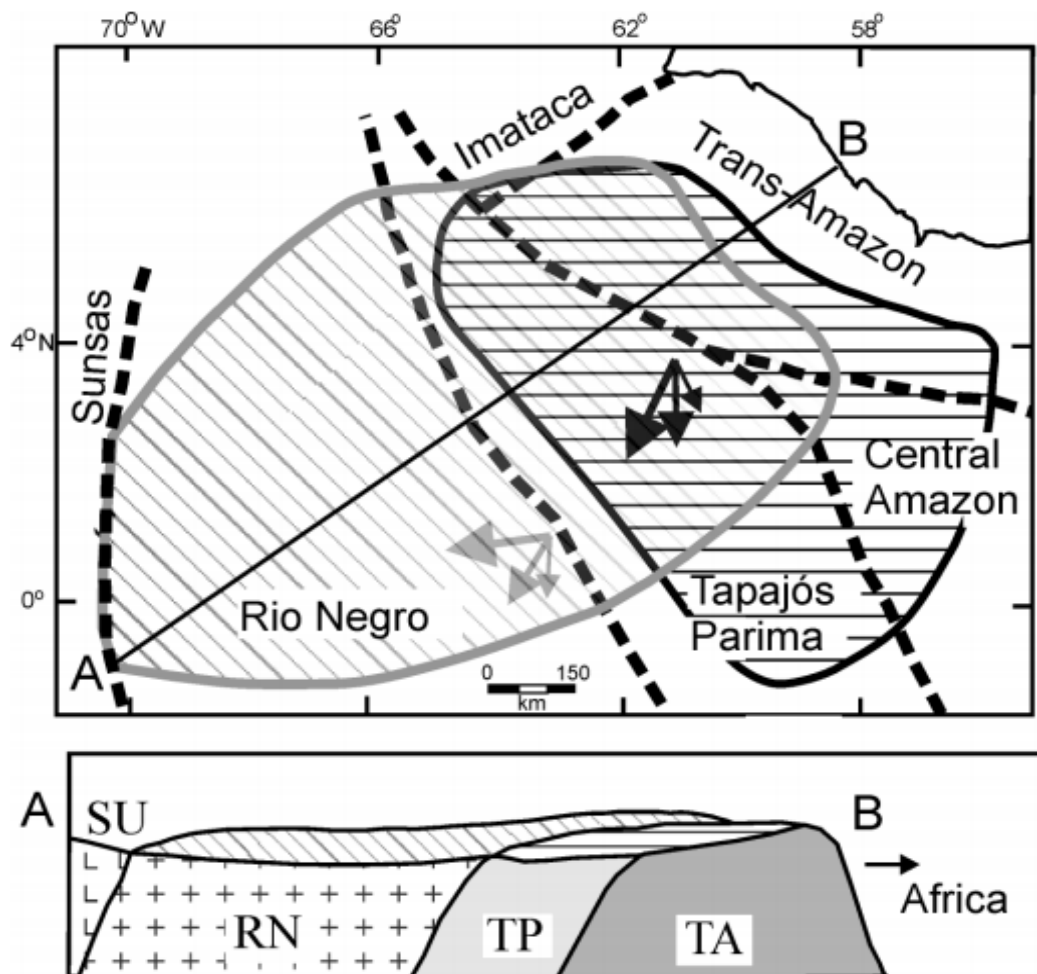

Figure 3. Location of the Roraima (inclined gray lines) and Neblina (horizontal black lines) sedimentary basins in relation to the geologic provinces of the Amazon craton: -Imataca; TA—Trans-Amazon; -TP—Tapajo-Parima ; -Central Amazon; -RN—Rio Negro and SU—Sunsas. (Modified from Santos et. al. 2003).

-Imataca/Bolivar province (3.5-2.7 Ga); high-grade metamorphic rocks (up to granulite facies) with several superimposed folding events, mainly felsic and mafic gneisses, banded iron-formations, marble and anorthosite. This province represents the root of this part of the craton.

-Pastora/Esequibo Province(2.6-2.1 Ga); plutonic, volcanic, and sedimentary rocks, metamorphosed to amphibolite facies;

-Cuchivero/Amazonas province (2.1 Ga); felsic volcanic and plutonic rocks, minor proportions of sedimentary rocks, all metamorphosed to greenschist facies.

-Roraima/Canaima province (1.8-1.4 Ga); Composed by clastic sediments (sandstones, quartzites, conglomerates) and siliceous rocks (chert, jasper), it was intruded by diabase dikes and sills. These rocks were affected by a slight static metamorphism, and outcrops in the Gran Sabana region.
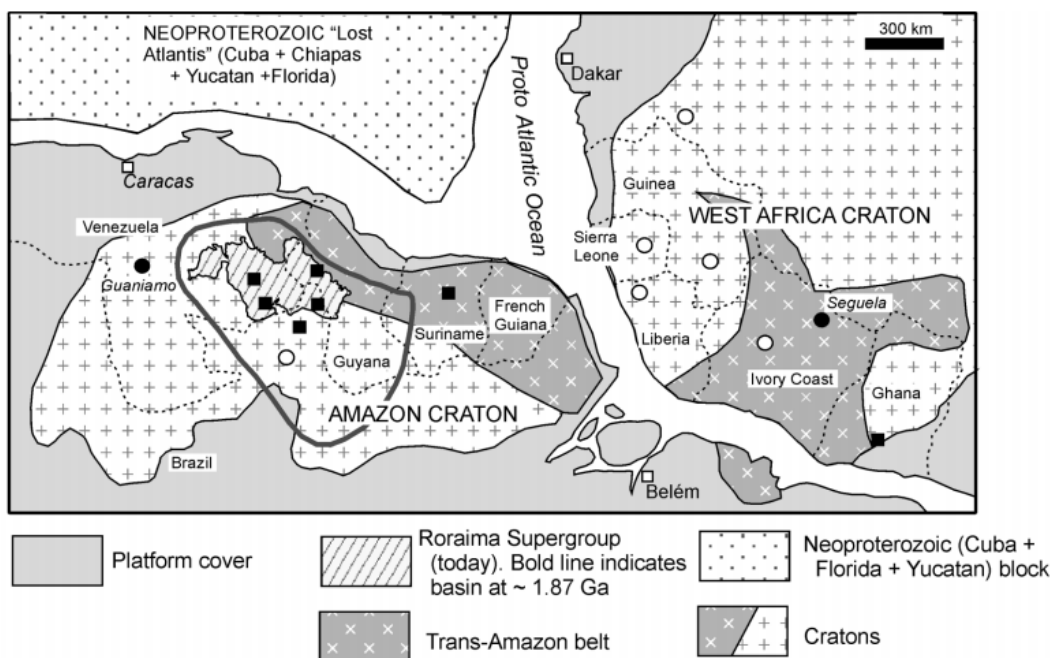
Figure 4. Extension of Roraima supergroup and position of Amazon Craton in the Mesozoic Gondwana continent (from Santos et. al. 2003).

A new different interpretation comes from Santos et al. (2000, 2003); according to these authors, the Roraima supergroup lays down over the northern part of Amazon Craton, which is divided in 6 geologic provinces; the Archean Imataca province and the Proterozoic Trans-Amazon, Tapajo´s-Parima, Central Amazon, Rio Negro, and Sunsas provinces.

1.2.1 Stratigraphy of Roraima supergroup

The Roraima group forms the table mountain cropping out in the area of study: the name comes from Roraima Tepui, famous for being of inspiration to Arthur Conan Doyle's novel "The Lost World", located at the triple border between Venezuela, Guyana and Brazil. This sequence was deposited in a large paleoproterozoic foreland basin (Reid, 1974). Rocks of the Roraima Supergroup consist principally of sandstones derived from the erosion of Trans Amazonian Mountains to the north, and deposited in braided, deltaic and shallow marine environment (Reis et al., 1990). Geographically, it covers 73000 km^2 in the northeastern part of Roraima state of Brazil (Reis et al., 1990), southeastern corner of the Bolivar State of Venezuela and northwestern part of Guyana. Division of Roraima group in sub-units has changed throughout time, since the first attempts of Dalton (1912). Then, it is evolved in a new subdivision done by Reid (1972) and Reid and Bisque (1975), following stratigraphic and paleoenvironmental criteria. They suggest four different formations, from oldest to youngest:

-Uraien Formation (>850 m) polymictic conglomerates to siltstones and fine-grained sandstones, siltstones and shale, unconformably overlying rocks of the Pastora and Cuchivero Provinces. It forms extensive monoclines and was intruded by diabase along the lower contact. The depositional environment is postulated as river bars and anastomosing channels, with southeast and southwest paleocurrent directions.

-Kukenan Formation (50-400 m) consists of easily erodible shales and siltstones, leading some previous authors to doubt its existence (Yanez, 1985; Simon et al., 1985). Its depositional environment seems to have been a large epicontinental sea or basin.

-Uaimapue Formation (up to 650 m) consists of quartzitic sandstones, volcaniclastic sandstones, quartzitic wackes subarkoses, arkoses, and tuff. It forms the conspicuous mono- clines of the lower parts of the table-mountains. Its depositional environment is postulated to be anastomosing channels with dominant southwest and west paleocurrent directions.

-Mataui Formation (600-900 m) consist of a cross-bedded massive quartzitic sandstones and wackes, lithic wackes and subarkoses, with abundant crossbeddings. It represents the youngest deposit of Roraima group, situated in the highest stratigraphic position, and forms the prominent part of the outcrops. Quartz normally represents over 80% of the rock, with well sorted grains, commonly between 30 and 100 μm in diameter, cemented with microcrystalline quartz (Sauro, 2014). Minor phyllosilicates as kaolinite, pyrophyllite and muscovite are included in the rock (Martini, 2000, 2004; Aubrecht et al., 2011), suggesting a low-grade metamorphism of Mataui sandstone; to generate pyrophillite from quartz and kaolinite the metamorphic reaction requires at least 3000 meters of burial (Turner and Verhoogen, 1960, p. 552), sediments that have been eroded during uplift (Briceno, 1990).

A different modern stratigraphic division has been recently summarized by (Reis and Yanez, 2001): From bottom to top, the supergroup is composed of the following units: Arai, Suapi (which includes the following sub-units: Uiramutà, Verde, Paure, Cuquenan, Quino), Uaimapue and Mataui.

A stratigraphic section of Roraima supergroup, designed on the base of this last subdivision, is shown in the figure 5.
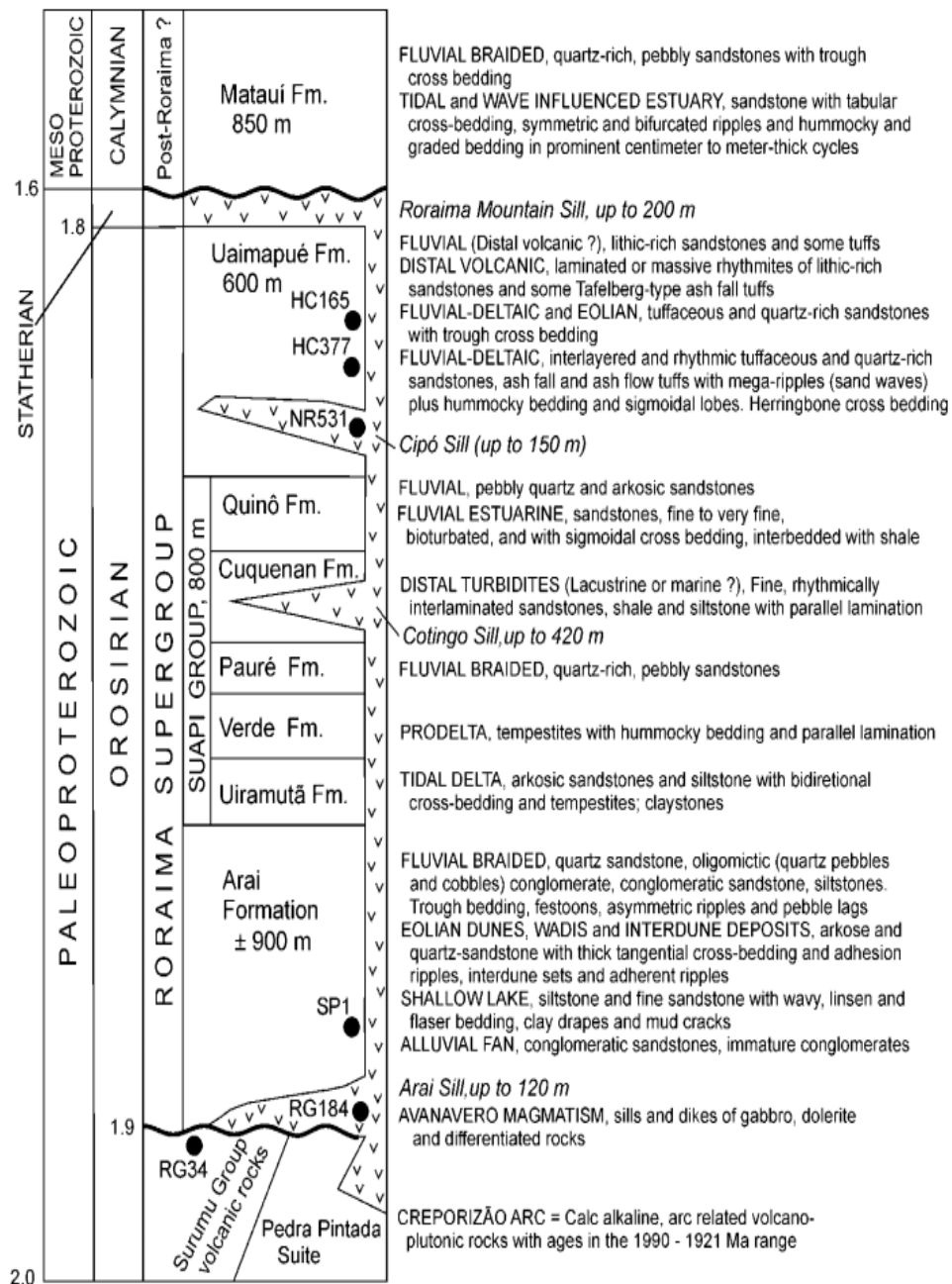
Figure 5. Roraima supergroup stratigraphy, according to Santos (Santos et.al., 2003; modified from Reis and Yanez, 2001).

Despite it is a valid schematic representation of an overall Roraima - stratigraphic trend, it might differ in some details from place to place: specifically either in the areas of Auyan Tepui and Chimantà massif, position of diabase dykes and sills in the stratigraphic column seems not coherent with this representation.

1.2.2 Isotopic dating

The age of this arenaceous group represents a big issue, since no fossils have been found. A relative dating can be inferred on the absolute dating of the granitic basement (2.3-1.8 Ga) and of the diabasic dykes and sills that intrudes the upper Roraima Group: isotopic K/Ar dating on this intrusion range from 1.4 to 1.8 Ga (Teggin et al., 1985), (Santos et al., 2003) and this might represent a likely minimum age . Direct dating on the ash-fall tuffs interlaying Uamaipuè formation can give information of the middle sequence of Roraima Group: several attempts were made in different places using Rb-Sr method, and yield ages of 1655 ± 19 Ma (Priem et al. 1973) for Suriname samples; in Venezuela, samples of the Canaima tuffs were dated 1747 ± 49 Ma (Gaudette and Olszewski, 1985).

1.2.3 Intrusions

As we previously mentioned, the Roraima group is cut by Precambrian diabase dykes and sills, intruded at different levels, cropping out until the upper Mataui formation; evidences of this are present in either Auyan and Chimantà massifs. Petrographically, the diabases consist of ortho- and clinopyroxenes, labradorite, and minor quantities of amphibole, chlorite, biotite and opaque minerals. The emerging part of this is subjected to alteration and pedogenesis (Briceno 1990). Moreover the group is also intruded by Mesozoic diabases, associated with the opening of Atlantic Ocean (Hawkes, 1966; Teggin et al., 1985). These form thin NE-trending dikes with ages around 200 Ma.

| Table 1. Major element analysis (in %) of diabases from the Chimantá Massif.								
Locality	Al_2O_3	CaO	Fe_2O_3	K_2O	MgO	Na_2O	SiO_2	LOI
Acopán	11.89	10.43	12.10	0.91	7.01	1.87	48.38	0.36
Toronó (1)	20.27	10.53	10.40	0.93	7.08	2.01	50.18	0.20
Toronó (2)	20.78	10.63	11.93	0.94	7.66	1.81	47.53	0.22
Toronó (3)	19.34	10.47	12.17	0.86	7.34	2.13	49.54	0.20

LOI, loss on ignition

Figure 6. Quantitative chemical analysis of the diabase, sampled on the Chimantà Massif (From Briceno, 1993).

1.2.4 Structural setting

Tectonic studies in Guyana Shield, and specifically in the table mountain area (Briceno 1982; Briceno and Shubert, 1985), shows that Roraima Group has been slightly deformed. Broad folds are present at large scale, large amplitude synclines and anticlines with approximately N/S and NW/SE trending axes; apparently, the main stress direction is oriented NNE/SSW (Briceno 1990).

The stress field that originates this slight deformation is still poorly unknown, and only few papers deal with this topic. The bedding is normally horizontal, in some cases slightly inclined; moreover, topographic inversion is a common feature, since most table-mountains are remnants of doubly-plunging synclines. Important regional faults with relevant displacement have not been observed in the Gran Sabana area (Gibbs & Barron, 1993), but surfaces of both Auyan Tepui and Chimantà massif are crossed by multiple sets of fractures, characterized by vertical dip and without considerable displacement. This set of joints intersects in a wide extended network and form a pattern of regular polygonal prisms. Some fractures, although even those do not show displacement, seems not be related with the joint network, because of their different orientation and length. The flat-top shape of the tepuis reflects the presence of erosional surfaces: according to Briceno and Shubert (1993), six different planation surfaces have been recognized

in Guyana Shield, based on the extension of flat areas having approximately the same elevation.
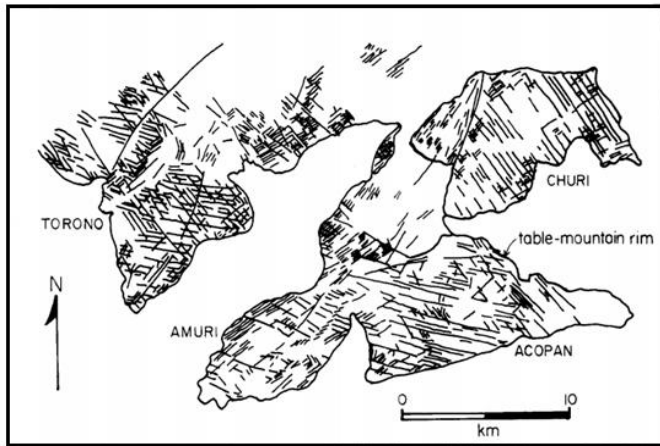
Two of these are the main responsible of shaping the Gran Sabana, and are clearly recognizable in our area of study. The Wonkèn surface, with an elevation of 900 - 1200 m, represents the main surface that forms the low, vegetated areas surrounding tepuis, and it has been formed on rocks of Roraima Group. Instead, the flat top surfaces of either Auyan Tepui and Chimantà massifs, carved in the Precambrian quartzite, are remnants of the same plateau, the "Auyan tepui planation surface" which stands at an elevation of 2000 - 2900 m a.s.l. and rise more than 1000m above the Wonkèn lowland. The age of this planation surfaces is still controversial: a reasonable, but still speculative, Mesozoic or older age of initiation can be assigned (Briceno and Schubert, 1993).

1.2.5 Morphology of tepuis

From a geomorphologic point of view, the upper plane of Tepuis is strongly influenced by joints: the network of fractures controls the drainage of surface water, which are the one of the causes of desegregation and differential erosion of the outcrop. Since the joints are mainly vertical, erosion proceeds in the form of collapse of blocks defined by joints and bedding planes, and thus the table-mountain topography is maintained (Briceno and Shubert, 1993). Chemical weathering is of a primary importance in creating particular landforms, usually peculiar of calcareous environments as karren, towers and pinnacles, stone forest and caves, that lead us to define it as a karst - like landscape (Urbani, 1986, 1990; Piccini, 1995). Areas interested by the presence of intrusions are usually highlighted by the presence of rounded, smooth topography, covered by dense and lush vegetation (Briceno, 1990).
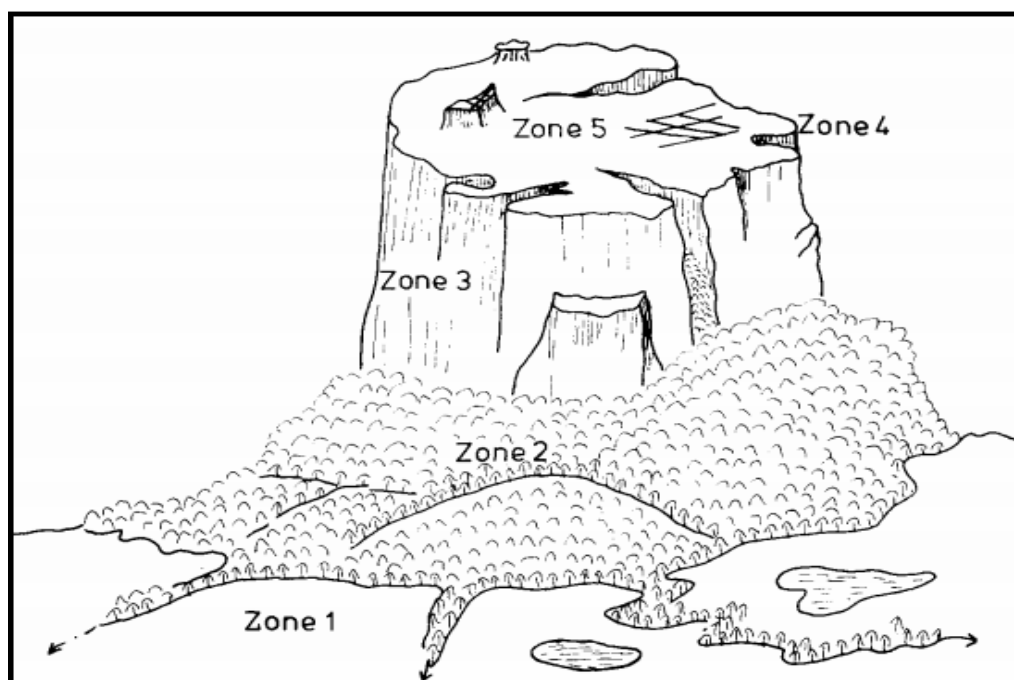
Figure 8. Schematic representation of table-mountain morphology: -1)Pediment-2) Foothills; -3)Scarp; -4)Rim; -5)Summit. (from Briceno and Schubert, 1993; modified from Pouyllau and Seurin, 1985).

The summit plateau of the tepui is rimmed by a cliff, which rise above the surrounding lowland and can reach considerable heights (up to 600 m); sometimes an inner scarp is present, with heights in order of tens of meters, which divides the surface of the tepui in 2 distinct plans. The base of the cliff is separated from the plain by the foothills, a series of gentle slopes formed by erodible rock layers, screes and alluvial fans.

2. Raw Data

The starting point to perform work using satellite images, is to verify the actual availability and completeness of raw data on the study area. The acquisition of high-resolution images by commercial companies was discarded for budget reasons, since the area that needs to be covered is extremely wide and it would lead to cost in addition. A regional study like this one, does not need a spatial resolution at the meter scale, for which a decameter scale it may be sufficient: therefore, we carried out a image search on the browsers of the major space or government agencies, which usually have an archive of free-download images.

## 2.1 USGS Data store and EarthExplorer

Earth Explorer is a USGS (United States Geological Service), browser that allow us to search and order satellite images, aerial photographs, and cartographic products from several sources, such as Landsat/Aster missions, NASA Terra and Aqua missions, Aster DEM etc.

EarthExplorer search criteria requires coordinates, addresses or polygon enclosing the area of interest, and the type of data; all the results available for the download are listed in the left box. For each file, there is the possibility to display the preview, the image footprint, or to access the specific product information, as cloud cover, acquisition time, orbit and meta-data attributes. Specifically, here we downloaded Landsat 8 image and the digital elevation model ASTER_GDEM of the Tepui area.

2.2 Landsat 8 image

Landsat 8 is a United States Earth observation satellite launched on February 11, 2013, the eighth spacecraft in the Landsat program. It was originally called

Landsat Data Continuity Mission (LDCM), and developed in collaboration between NASA and USGS.
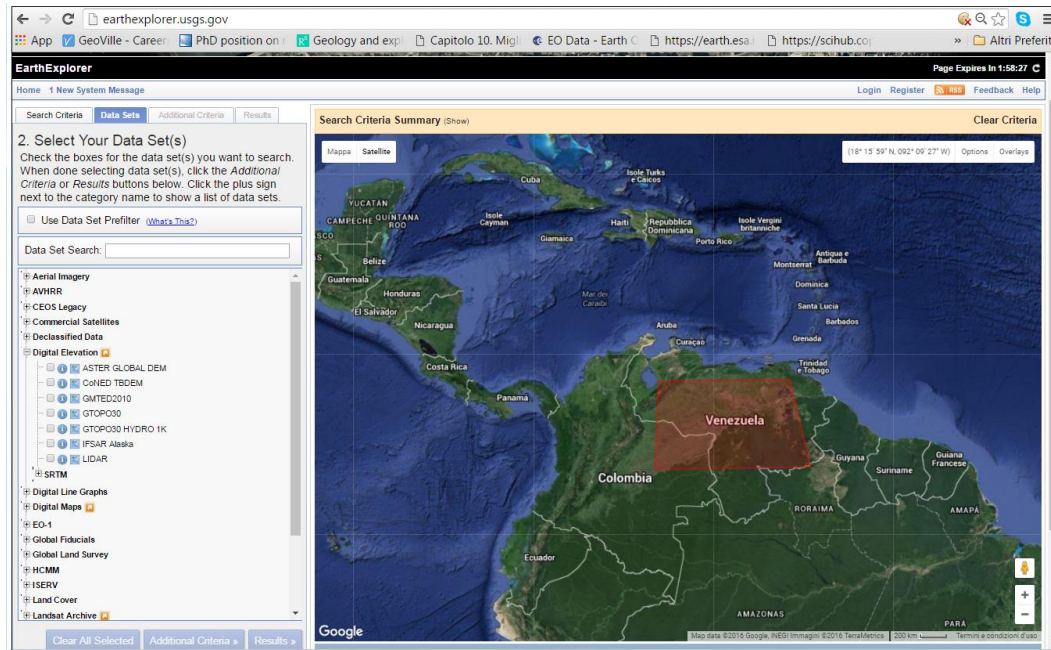
Figure 9. Example of EarthExplorer window, with the selected area (red polygon) drawn on the map, and the available dataset listed leftward.

Landsat 8 will ensure the continuation of acquisition of Landsat data, utilizing two different sensors: the Operational Land Imager (OLI), and the Thermal InfraRed Sensor (TIRS), provided with two thermal bands.

Respectively, these two instruments will collect image data for nine shortwave bands and two longwave thermal bands. The file size is approximately 1Gb compressed. The pixel size, that correspond to the spatial resolution, is of 30 m in the visible (bands 1-3), near and shortwave infrared (bands 4-7) and cirrus bands, and 15 m in the panchromatic. Thermal bands 10-11 are collected at 100 meters pixel resolution, but resampled to 30 meters to match OLI multispectral bands.

OLI bands:

Spectral Band	Wavelength	Resolution
Band 1 - Coastal / Aerosol	0.433 - 0.453 µm	30 m
Band 2 - Blue	0.450 - 0.515 µm	30 m
Band 3 - Green	0.525 - 0.600 µm	30 m
Band 4 - Red	0.630 - 0.680 µm	30 m
Band 5 - Near Infrared	0.845 - 0.885 µm	30 m
Band 6 - Short Wavelength Infrared	1.560 - 1.660 µm	30 m
Band 7 - Short Wavelength Infrared	2.100 - 2.300 µm	30 m
Band 8 - Panchromatic	0.500 - 0.680 µm	15 m
Band 9 - Cirrus	1.360 - 1.390 µm	30 m

Thermal infrared sensor bands (TIRS) :

Spectral Band	Wavelength	Resolution
Band 10 - Long Wavelength Infrared	10.30 - 11.30 µm	100 m

Band 11 - Long Wavelength Infrared	11.50 - 12.50 µm	100 m

General Data Characteristics:

- GeoTIFF data format;

- Universal Transverse Mercator (UTM) map projection;

- World Geodetic System (WGS) 84 datum;

- 12 meter circular error, 90% confidence global accuracy for OLI;

- 41 meter circular error, 90% confidence global accuracy for TIRS;

- 16-bit pixel values of radiometric resolution.
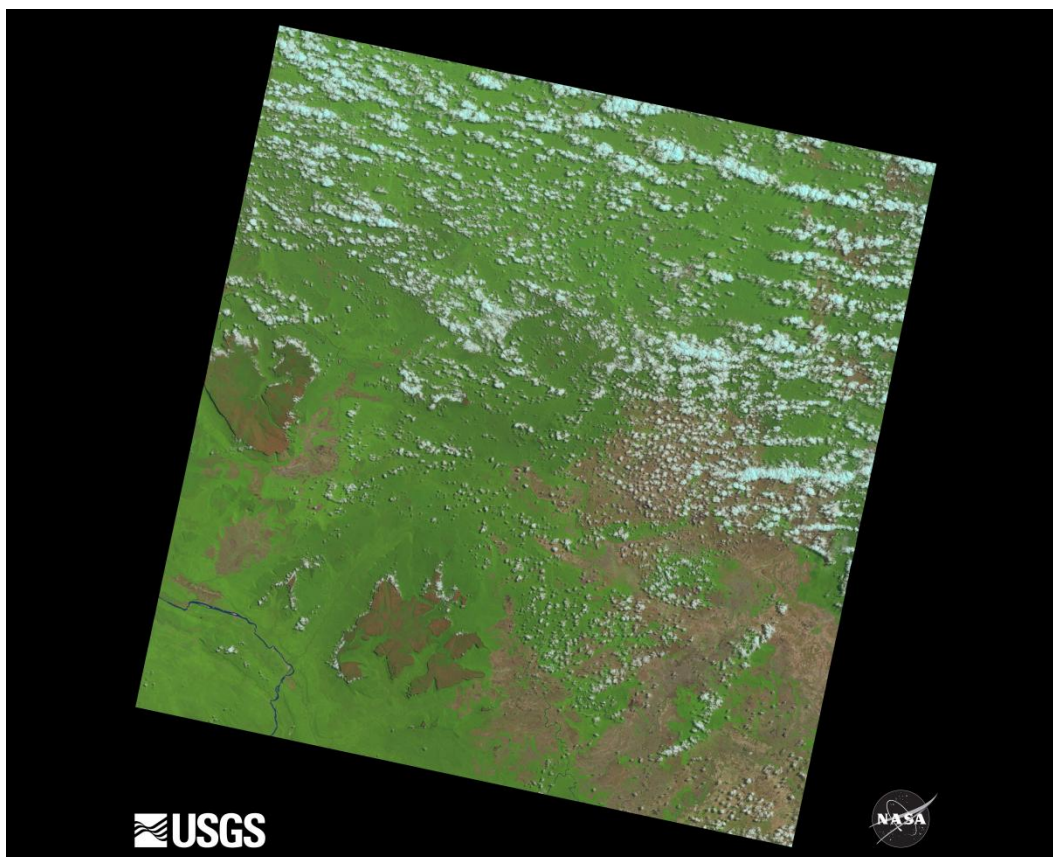
Figure 10. Satellite image that includes our area of study: Tepuis are visible in the lower-left corner. N.B. the orientation is "North_UP". (Image courtesy of the U.S. Geological Survey.)

In the specific, the metadata that we downloaded has been collected on the 2015-05-04 at 20:35:16, georeferenced in WGS_84, UTM_Zone 20, with a cloud cover of 18.21 % that interest only marginally our area of study (fig.2).
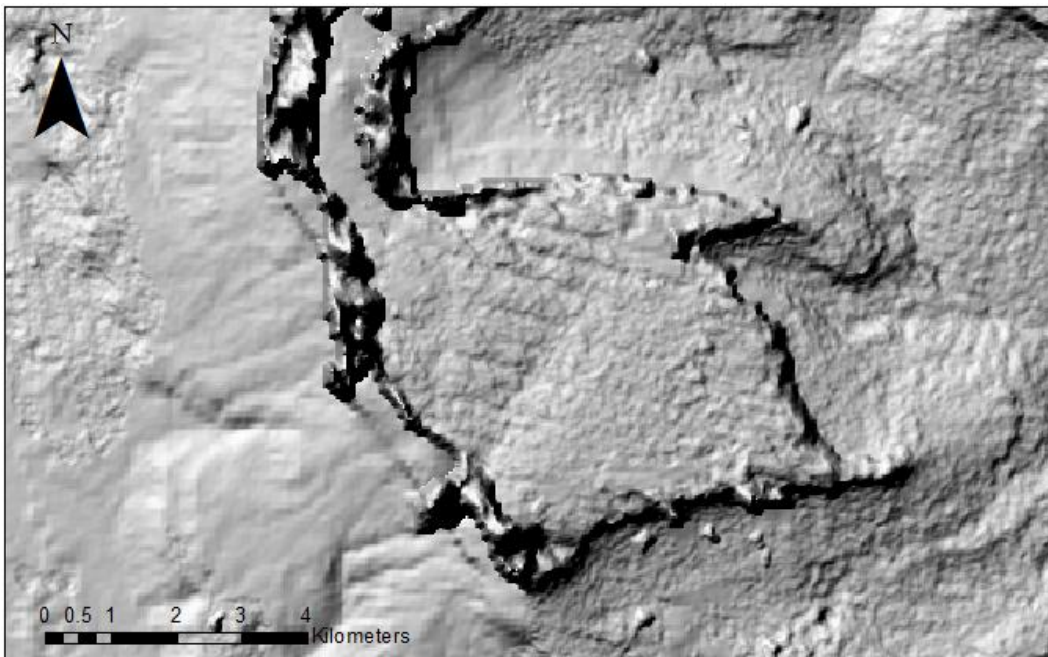
2.3 Aster G DEM

Aster, acronym of Advanced Spaceborne Thermal Emission and Reflection Radiometer, is a Japanese (developed by METI, Ministry of Economy, Trade, and Industry) sensor devices on board of Terra satellite, launched into Earth orbit by NASA in 1999. It provides image data used to create detailed maps of surface temperature of land, emissivity, reflectance, and elevation. In particular, thanks to its stereo-channel system, it has provided a Digital Elevation Model covering the entire land surface of the Earth (from 83° North to 83° South) at high resolution (15m VNIR, 30m SWIR, 90m TIR), and is available at no charge to users worldwide. ASTER Global Digital Elevation Model was created by compiling 1.3 million VNIR (visible and near-infrared) images taken by ASTER using single-pass stereoscopic correlation techniques, with terrain elevation measurements taken globally at 30 meter intervals.

Figure 11. Example of raw Aster G-DEM files.

However, some reviewers argue that the true resolution is considerably lower, and sometimes the quality is affected by the presence of systematic error patterns (e.g. DEMs can includes artificial structures, that are systematically too low or high and therefore not representative of terrain's surface) (Hirt et al., 2010). The DEM we used is affected by some defect caused by cloud disturb, which are displayed as topographic reliefs (fig.4).


Figure 12. Detail of the hillshaded Aster G_DEM of Abacapa Tepui, located in the Chimantà Massif: the clouds are falsely represented as reliefs.

2.4 ESA Copernicus

The dataset available on USGS browsers, as EarthExplorer and Glovis, mainly refer to the missions sponsored by NASA, such as Landsat and Aster we mentioned above; other recently collected satellite images can be found on the European Space Agency website (ESA). In 1998, with the aim to replace and expand the Envisat mission (active 2002-2012), the European Space Agency started the preparative phase of the project Copernicus, which became fully

operational in the biennium 2014-15. It is the largest single earth observation program in the world, and aims to provide accurate and easily accessible information useful to environmental management and to understand the effects of climate change. As part of the Copernicus Program, the Sentinel program consist of 7 satellite missions (some of them will be launched in the near future) including radar (Sentinel-I) and hyper-spectral imaging (Sentinel-II). The data are available free of charge, upon registration, from the website of ESA. The search method is very similar to that seen previously for EarthExplorer website; a data hub (https:// scihub. copernicus.eu/dhus/#/home) allows you to set the usual parameters of our search (area of interest, type of data, date of acquisition etc.) .
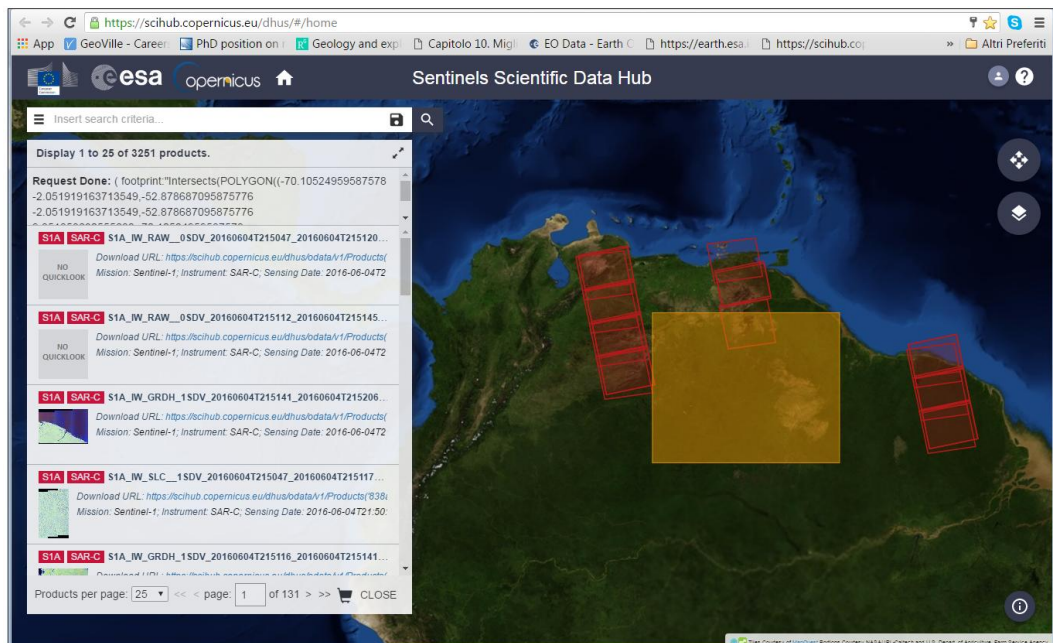
Figure 13. Example of ESA-Copernicus Sentinels scientific Data Hub, with the selected area (yellow polygon) drawn on the map, the available datasets (listed leftward) and their footprints (red polygons) .

2.5 Sentinel II

Sentinel-II project has been developed to perform terrestrial observations for land monitoring and natural disaster management, in the context of the Copernicus

Program. It includes twin polar-orbiting satellites in the same orbit, phased at 180° to each other (called Sentinel 2-A and Sentinel 2-B), with a coverage limit from 56° latitude south to 84° north; the orbit is 786 km of altitude, with 290 km^2 field of view. Both these satellites are equipped with a single multi-spectral instrument (MSI) with 13 spectral channels in the visible/near infrared (VNIR) and short wave infrared spectral range (SWIR), with spatial resolution of 10 m, 20m and 60 m.

Sentinel II band list:

Sentinel-2 Bands	Central Wavelength (µm)	Resolution (m)
Band 1 - Coastal aerosol	0.443	60
Band 2 - Blue	0.490	10
Band 3 - Green	0.560	10
Band 4 - Red	0.665	10
Band 5 - Vegetation Red Edge	0.705	20
Band 6 - Vegetation Red Edge	0.740	20
Band 7 - Vegetation Red Edge	0.783	20
Band 8 - NIR	0.842	10
Band 8A - Vegetation Red Edge	0.865	20

Band 9 - Water vapour	0.945	60
Band 10 - SWIR - Cirrus	1.375	60
Band 11 - SWIR	1.610	20
Band 12 - SWIR	2.190	20

The Sentinel file we downloaded is very heavy, about 7.36 GB (decompressed) and it is divided in 13 parts named granules (each contained in a different folder) . Each of these 13 folder contains the metadata, the image file and some other auxiliary information, as the quality indicators and the report. The cloud cover percentage is 14.9 %, mostly concentrated far from the Tepui's area.
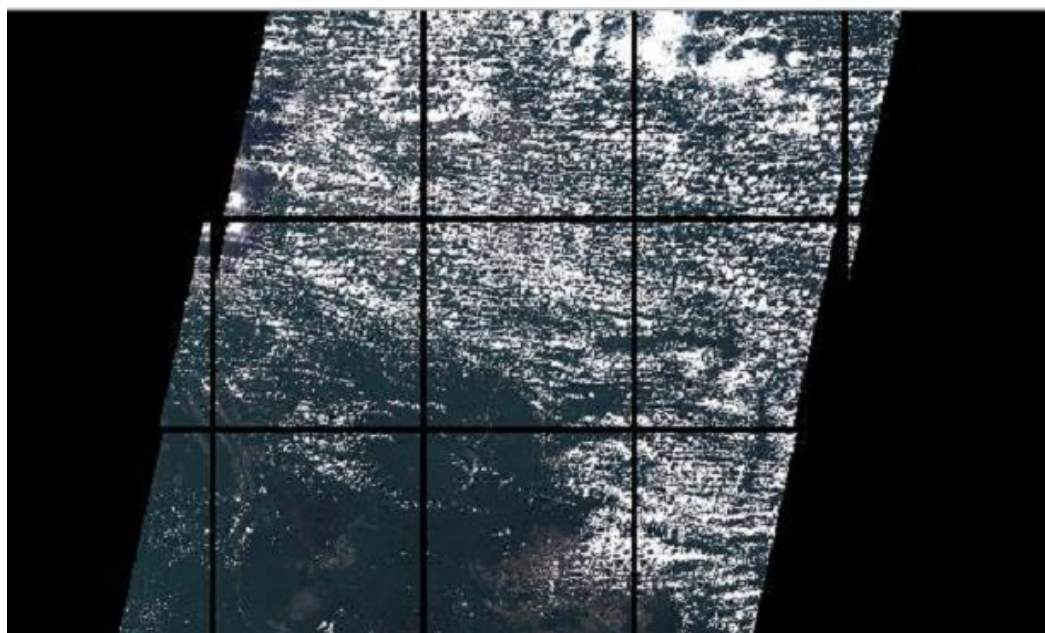
Figure 14. Mosaic with the 13 granules that compose the satellite image. Note that most of the cloud covering is concentrated in the northern part, while our area of study is located in the granule N.2 from down left.

The default coordinate system is WGS 84 - UTM zone 20, North and the date of acquisition is 2015-12-06, one of the more recent available. Since the surface covered by the complete Sentinel file is much wider than our area of study, only the folder containing the files of interest has been unzipped and used, in order to have a lighter data (580 MB, instead of the 6.7 GB of the complete file).
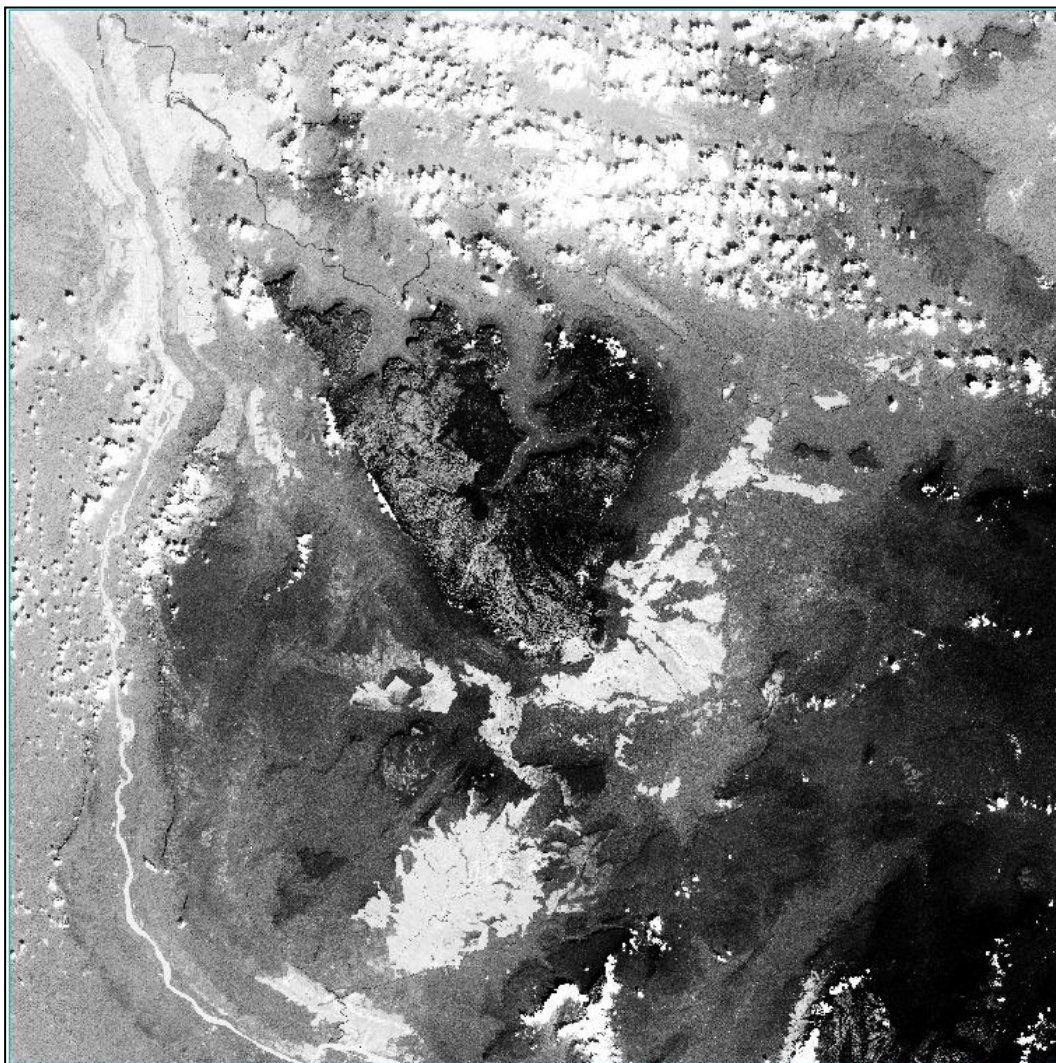
Figure 15. Sentinel Granule of the study area represented in Grayscale. Note that clouds do not influence significantly the tepui in the centre of the picture.

3. Data Processing

I have analyzed data coming from different satellite platforms. In particular I worked on :

- A Landsat 8 image, covering the Chimantà Massif and most of the Ayuan Tepui;
- A Sentinel II image of the Ayuan Tepui;
- A Aster G-DEM that covers the entire area of study.

The rough satellite images were preprocessed before the analysis and interpretation. All processings were carried out using ENVI 5.1 - software (**EN**vironment for **V**isualizing **I**mages) while the interpretations were accomplished in ArcGIS environment.

3.1 Layer stacking

Layer stacking allows to build a multi-band file merging georeferenced images of various pixel size and projections.**.**

Our satellite image folders (both Landsat and Sentinel) contain one file for each spectral band, hence to work on multiple bands using an unique file a layer stacking is needed. In particular all Landsat 8 bands were merged together, whereas three out of 12 sentinel II bands have been discarded (B.1- costal aerosol, B.9 -water vapor and B.10 SWIR-cirrus, all with 60 meter spatial resolution), because of the low resolution and unapplied on pluvial inland terrains

The output merged file were resampled and re-projected to new parameters. In particular**,** I chose the highest spatial resolution of the bands available for each satellite data (i.e. 15 meters for Landsat and 10 for Sentinel II) and I set the "WGS_84 - UTM Zone 20" as the output map projection. The resampling was

carried out applying the "nearest neighbor" method, which assigns to a pixel in the output grid the same radiance value of the closest pixel in the input grid. Indeed this algorithm maintains the same radiance values of the original image, but with a poor geometric accuracy. Finally the stacked files have been subset, removing the zones without remarkable informations. More in detail the area of interest has been overlapped with a polygon and then clipped with the ENVI tool "resize".
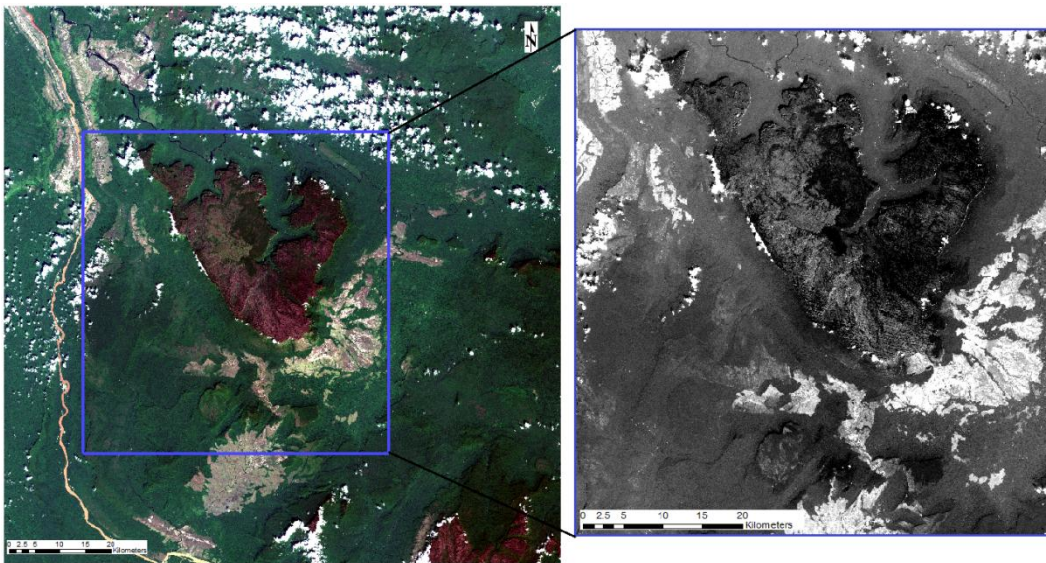
Figure 16. To the right, the stacked Sentinel II image, overlapped with the polygon that we used to resizing. To the left, the grayscale subset image representing the area of study.

3.2 Image sharpening:

Image sharpening is a processing method who allows the union of high resolution panchromatic layers with lower resolution multispectral layers; as a result, we obtain a multispectral high resolution false color image. Among the various sharpening methods provided by ENVI, I have selected the "Color Normalized Spectral sharpening" used to improve both the Landsat 8 and Sentinel II files. The Color Normalized Spectral sharpening can be applied on specific RGB false colors using a high resolution band to achieve the resolution sharpening.

However by repeating this operation many times, changing the RGB false color, we might sharp every spectral band of the input image. The bands are successively stacked into a single new multiband file.

3.3 Band Ratios

As a results of materials interactions with EM radiation, every object has a characteristic signature, displayed in a reflectance/wavelength graph as a succession of "peaks and valleys", with maximum and minimum levels of absorption throughout the entire spectrum. Band ratios consist in dividing the digital number-value (DN) of a pixel in a spectral band with the DN of the same pixel in another band.
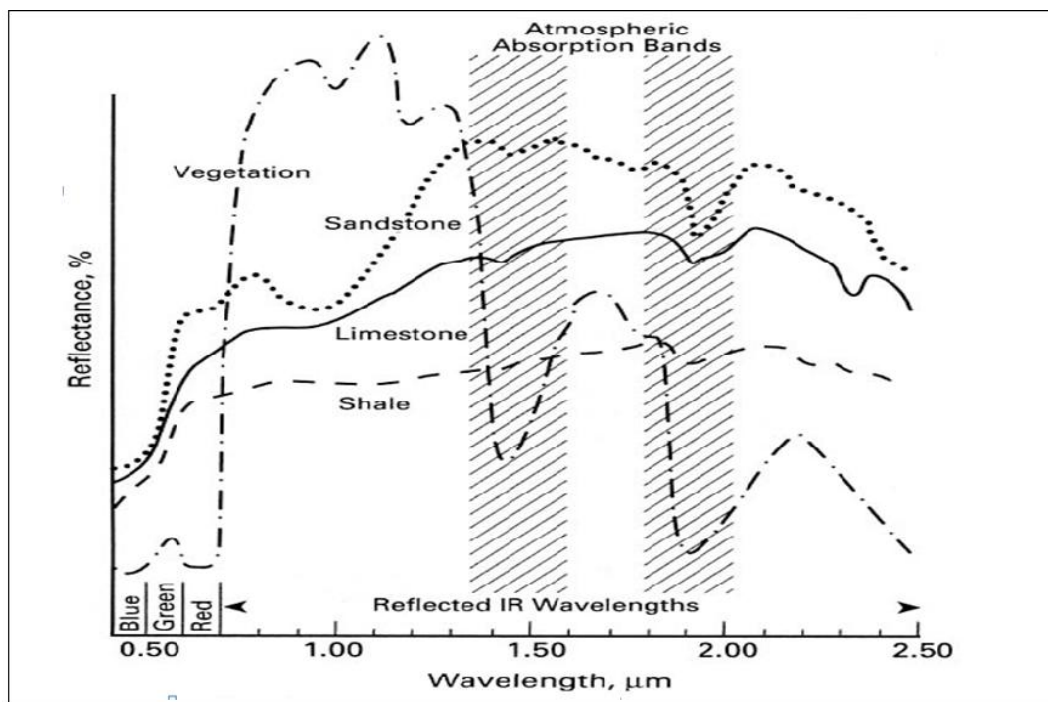
Figure 17. Spectral signatures of some common elements (vegetation and some rocks) where high levels of absorption ("valleys") and their adjacent shoulders are evident (Sabins, 1996).

This tool is useful in order to highlight several different materials by dividing shoulders of their spectral signatures with the nearby absorption peaks. For example on the classical Landsat 7 ETM data vegetation is highlighted by the 3/4 ratio (i.e. visible red/near infrared), ; clay minerals can be shown with the 5/7 ratio on short wavelength infrared ranges and oxides are typically highlighted through the spectral slopes expressed by the 3/1 band ratio (i.e. visible red / visible blue).

Note that random noise in different bands is often uncorrelated, and the ratio of spurious DN-values in either numerator and denominator produce extreme values, leading to an exasperation of noise that should be eventually cleaned through median filters (Drury, 1987).

### 3.3.1 Normalized Difference Vegetation Index (NDVI) and Vegetation Masking

The Vegetation Indexes are band ratios for detecting lands with different vegetation cover. As already mentioned before lush vegetation has a strong reflection in the near infrared (NIR)(0.8 -1 μm) and absorb radiation in the visible red (R), hence R /NIR ratio can be used to enhance its presence. Since this processing depends on the absolute values of R and NIR, it is strongly influenced by conditions on which data are collected (i.e. different atmospheric conditions and acquisition geometries), which might vary trough time. This prevents the use of R/NIR ratio in case of multi-temporal analysis. For this reason the Normalized Difference Vegetation index has been proposed and widely used in order to NDVI to overcome this problem. NDVI is defined as:

NDVI= [NIR - R] / [NIR + R]

NIR: near infrared

R: visible red

NDVI has been used to obtain a vegetation mask: on Sentinel data we used Band 3 for the visible red and band 6 for the NIR. The resulting band ratio is a grayscale image, where, in my case vegetation has values usually higher than 0.75. The mask were hence realized using this value as an upper threshold.
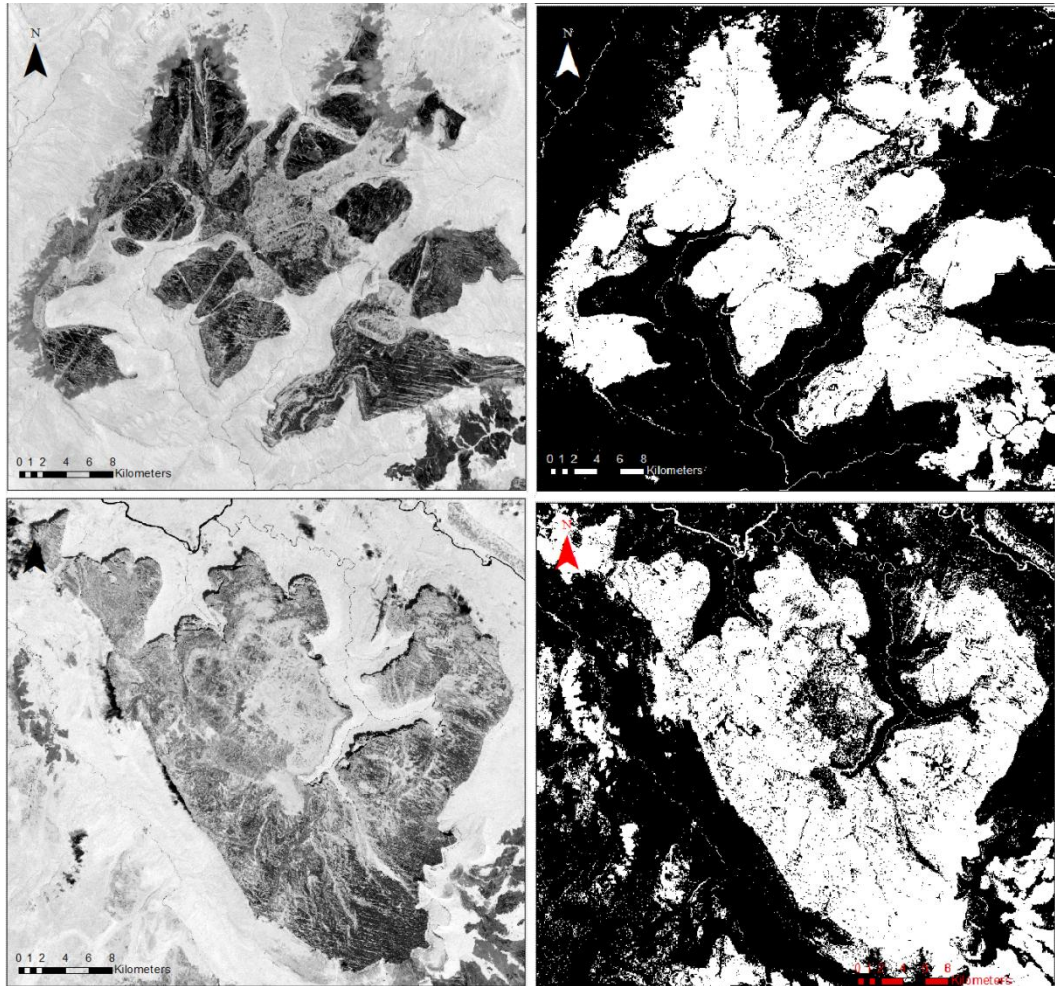
Figure 18. NDVI files and relative vegetation mask of Chimantà Massif (upper image) and Auyan Tepui (lower image), created from Landsat 8 and Sentinel II images respectively.

The same operation has been done with the Landsat 8 image but using a 4/5 ratio (equivalent to the standard 3/4 on Landsat 7 ETM) and, in this case, I get a value of VI for vegetation higher than 0.25 and I used this value as an upper threshold

mask on Landsat 8 data. The NDVI file have been also used to create the cloud mask: in this case I have removed the range of values from 0.17 to 0.21.
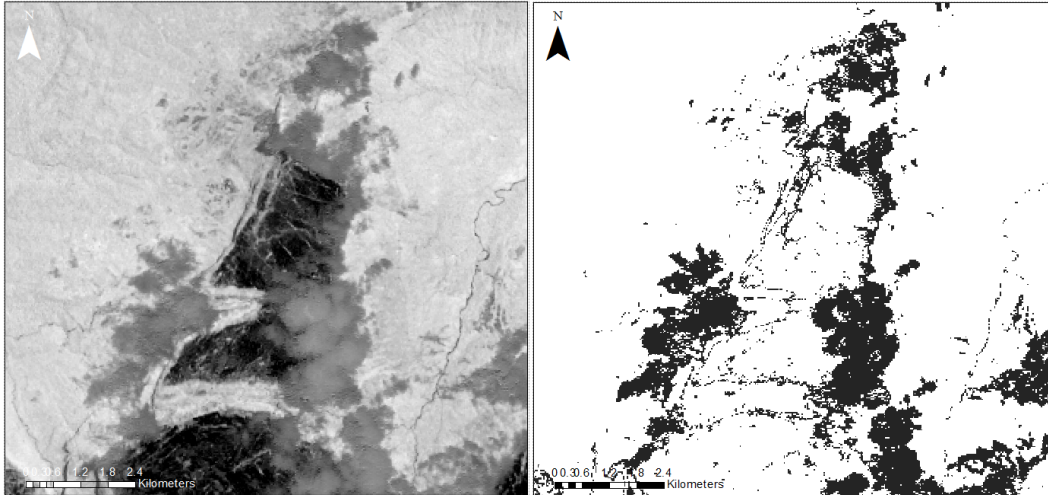
Figure 19. Detail of the NDVI file of the Chimantà Massif and cloud mask of the same area.

3.3.2 Detecting clay minerals

As we will see later, I am interested to verify the presence of clay minerals in the area of study, which can be indicative of argillitic alteration. In this case, the ratio has to be done using the peak of clay absorption at 2.2 µm as the denominator and the "shoulder" closer to the peak (around 1.6 µm) , as numerator.

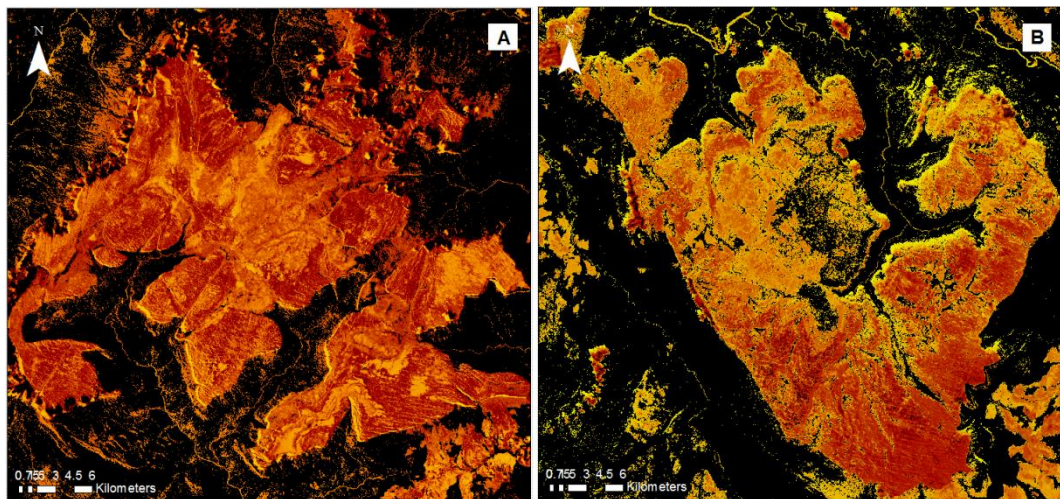As shown in figure 5 the band ratios used for Landsat 8 and Sentinel II images were respectively:

B6/ B7 = (SWIR1 =1.610 µm)/(SWIR2 = 2.2 µm)

B 11 / B12 = (SWIR1= 0.842 µm)/(SWIR2= 2.19 µm)

40
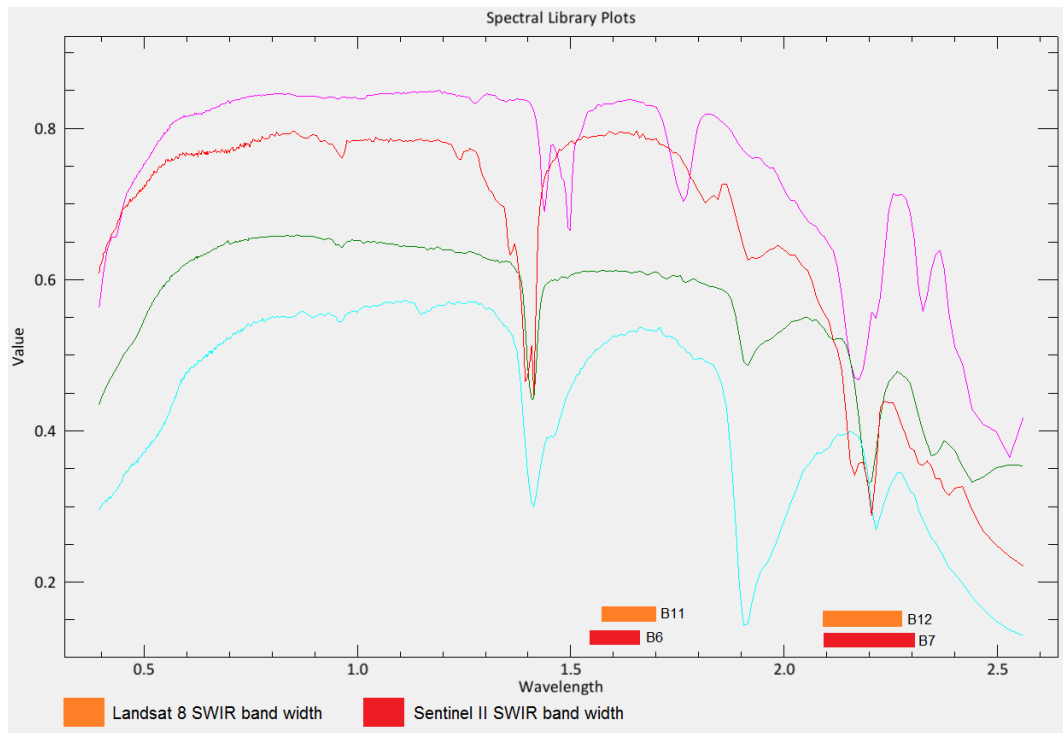
Figure 20. Reflectance spectra of some of the most common clay minerals (purple: Alunite; red: Kaolinite; green: Illite; blue: Montmorillonite), With the relative Lansat8 and Sentinel II bands used.

Figure 21. Masked "Clays map" of Chimantà Massif (figure A) and Auyan Tepui (figure B), based on Sentinel II and Landsat 8 images respectively. The colors have been changed using color slicing from grayscale to "red temperature", to enhance the presence of clays (highlighted by brighter colors) .
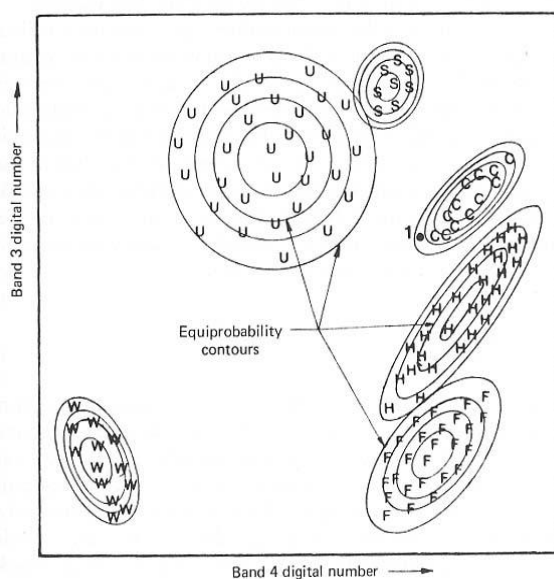
3.4 Image Classifications

The classification method relies on the fundamental concept of subdividing a set of data (pixels) in different classes, on the base of their clustering in a n-dimensional space where n is the number of bands of an image data cube provided by a given remote sensing sensor.

The classification methods are divided into two main groups:

Unsupervised Classifications: these are automatic classifications without the supervision of the operator and for which the real situation on the ground is assumed not be known. Classical classifiers for such operations are the IsoData and the K-Means classifier. Further details are not needed on such classification since I have not applied them during my work.

Supervised Classifications: these classifications need to be guided by the operator since they are based on the knowledge of some areas (training sites) representative of the surface classes. Supervised classification methods include Maximum likelihood, Minimum distance, Mahalanobis distance, Spectral Angle Mapper (SAM) Classification. Among these one, we opted for the *Maximum Likelihood Classification*.

Figure 22. Schematic representation of the Maximum Likelihood Classification method. (Lillesand and kiefer, 1994).
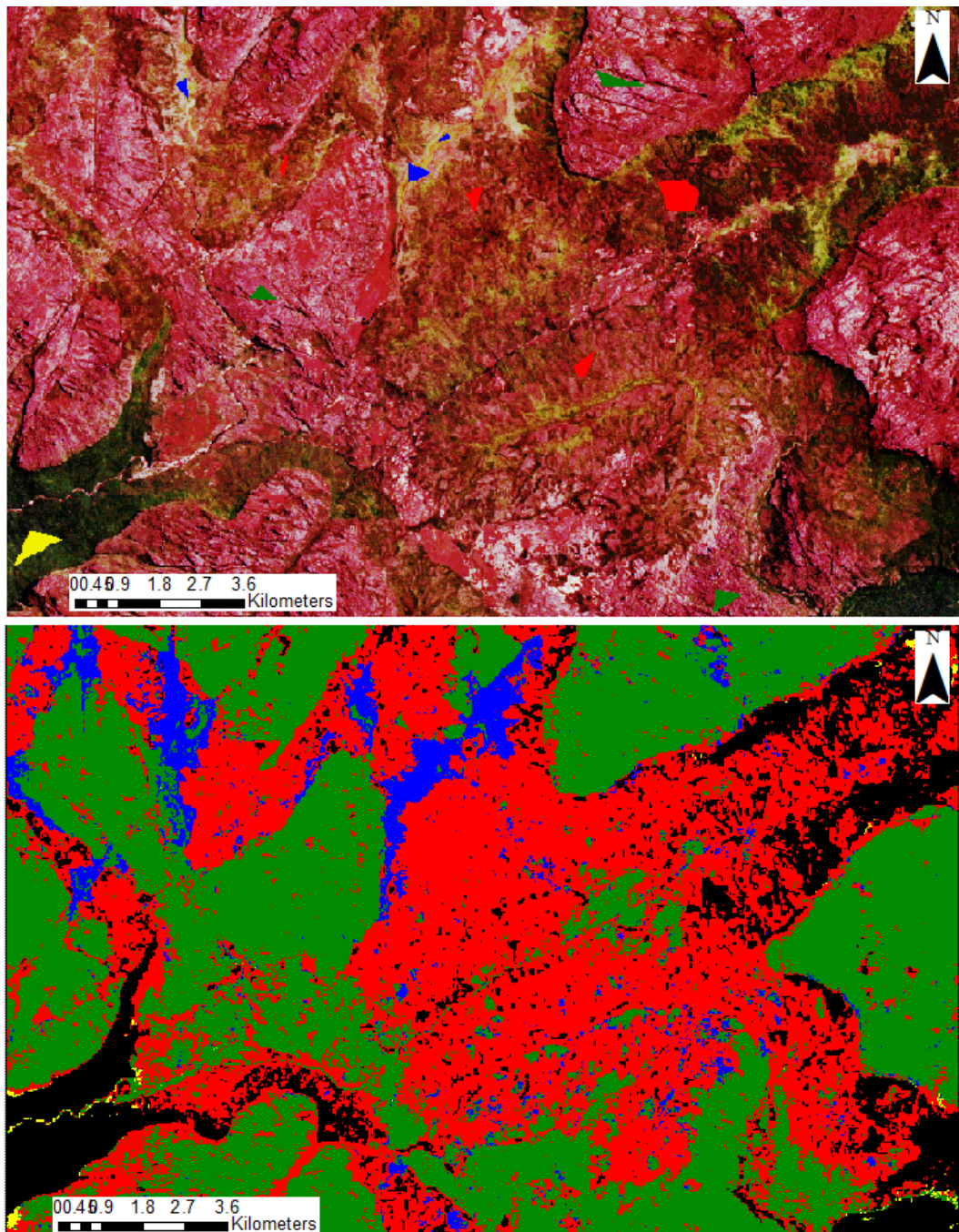
Figure 23. Above, detail of the stretched Landsat natural color image representing the central part of the Chimantà Massif, with the Region Of Interest. Specifically, the four class created are: vegetation (yellow); quartzite (green); diabase (red); alteration (blue). The image below represents a portion of the thematic map generated. Vegetation has been removed applying a Mask.

The Maximum Likelihood classification assumes that the statistics for each class in each band are normally distributed and calculates the probability that a given pixel belongs to a specific class. Each pixel is assigned to the class that has the highest probability (i.e. the maximum likelihood). This classification have been applied to both the Lansat8 and Sentinel II images. To proceed with this method, we have selected Region Of Interests (**ROIs**) on the images which were representative of the classes of interest and were used by the software as a "guide" to classify our dataset.

In particular the ROIs drew on the map, were representative of the various lithologies/elements present in the study area, such as the quartzite of the Mataui formation, the diabase intrusion and the alteration zone. The final classified maps were then used as further bases for the geological interpretation.

3.5 Digital Filters

The digital filters are floating windows or convolution operators that perform a linear and localized transformation on the image, allowing us to extract remarkable elements. The result of a filter operator to a pixel, depends on its value and on the values of the pixels belonging to its neighborhood. In particular, the value of a pixel is replaced with the result of one or more elementary operations, performed on the element itself and the elements of its environment. The coefficients of the function that acts on a pixel and its neighborhood are organized in the form of a matrix, called KERNEL, which can have different sizes (3 x 3, 5 x 5...). The kernel shifts over each image elements and its proximity, and the new pixel values are calculated on the base of the convolution between the two matrix. The output image has the same size of the input one, but the recalculation of every pixel value highlight different features according to the type of filter used.
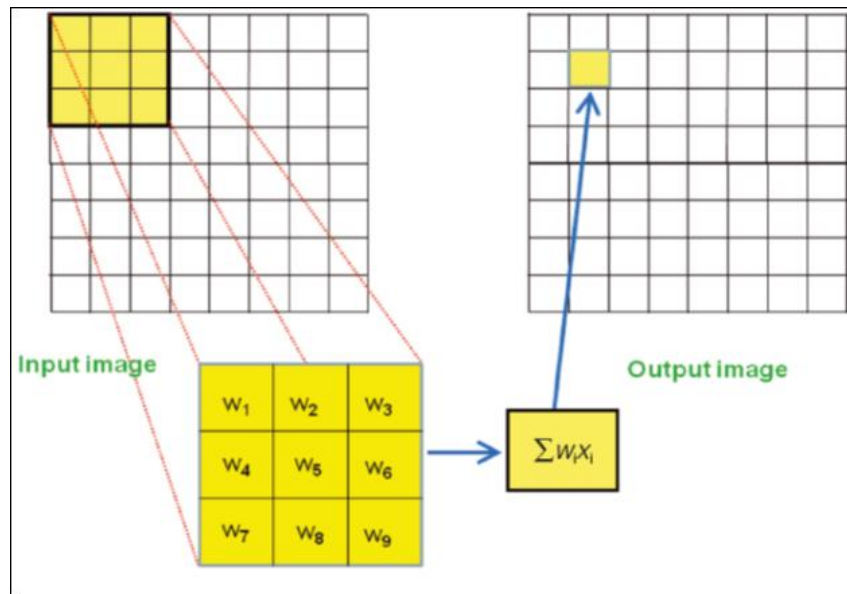
Figure 24. Schematic representation of a digital filter, with a 3 X 3 matrix. The kernel size is always an odd: the matrix is placed over a 3 X 3 patch of image pixels and the weight is multiplied by the associated central pixel value. From Mather and Koch (2011).

Filters can be divided in two main classes: **Low Pass Filters** and **High Pass Filters.** The first ones remove the high frequency part of an image and preserve the low frequencies and are used in order to smooth the image and recognize its high - scale background features. Conversely, High pass filters discard the low frequencies components of an image, and they are applied to highlight local low-scale details and variations. To collect structural data from our study area, it can be advantageous to emphasize lineaments and fractures from the rest of the image. Among the many type of filters available in ENVI, which rely on different algorithms (Laplacian, Directional, Gaussian, Median ecc.), the Directional ones are the one that suit best our purposes. As high-pass and low pass filters also the directional one are based on kernels whose coefficients are suitable for enhancing image edges. Edges are linear limits caused by the sudden variation of pixel values. They mainly depends on lightening conditions due to topography (azimuth, slope and orientation of the surface) and physical/chemical variations (mineralogy, texture of materials); therefore, detecting edges is a valid way to

identify all those characteristics. In particular they turned out to be very useful for fracturing detection. Using the directional filters, we selectively enhance image features depending on their specific direction.
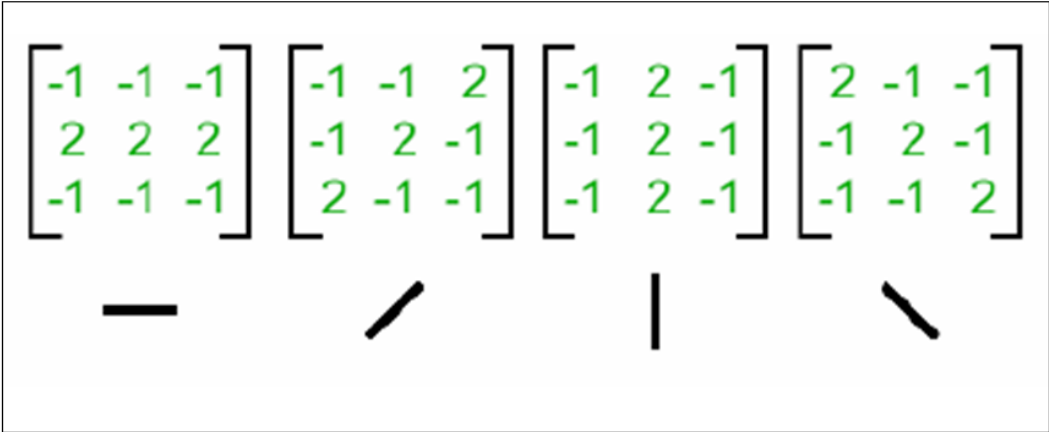

Figure 25. Typical directional edge enhancement kernels, with the respective directions of enhancement.
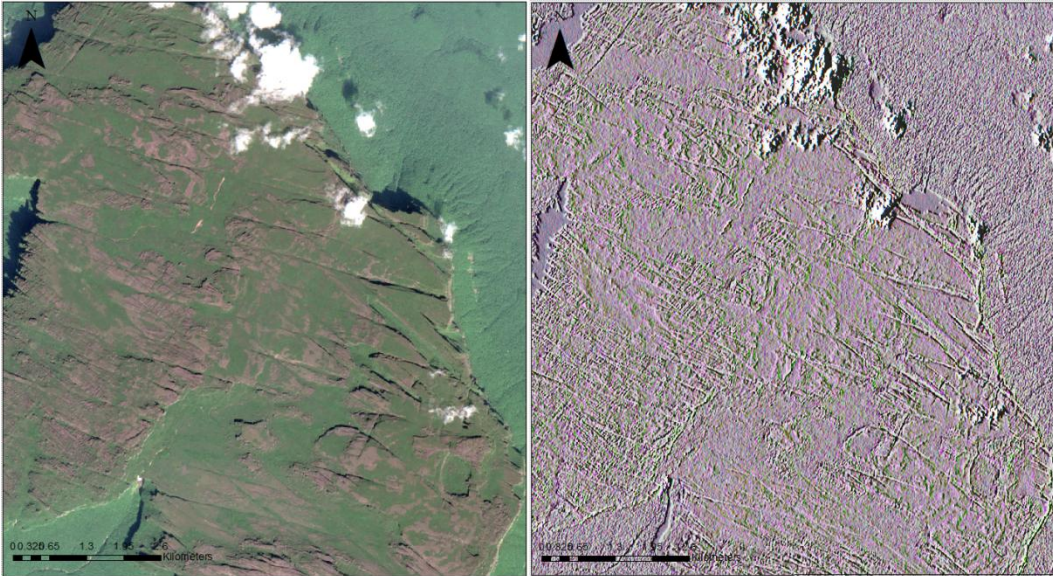

Figure 26. Example of use directional matrix, with horizontal directional filter angle.

3.6 Contrast Stretch

Contrast stretch is a crucial visualization tool during interpretation.

The pixels in a data file that make up an image can have any value (negative, positive, integer, or floating point). When the image data are visualized on a screen, pixels are displayed as brightness values: however a monitor can display only 256 level of brightness, ranging from 0 and 255 (where 0 is black and 255 is white). Contrast stretching consist in rescaling the data pixel into a range of values that can be displayed by the monitor. This process aim to expand the narrow range of values of an input image over a wider spectrum, increasing the difference between dark and bright pixels, changing the contrast in the image.

The stretch used to rescale image data into brightness values can make a drastic difference in the way that the image appears, enhancing the features in which I am most interested. ENVI has 9 different possibilities of contrast stretch, which rely on different rescaling algorithms.

I mainly used:

- Linear;
- Equalization;
- Gaussian;
- Optimized Linear;

In addition, other types of stretching are provided by the software Arc_GIS, where the files have been uploaded to the interpretation:

- Standard deviation;
- Histogram equalize;
- Histogram specification;
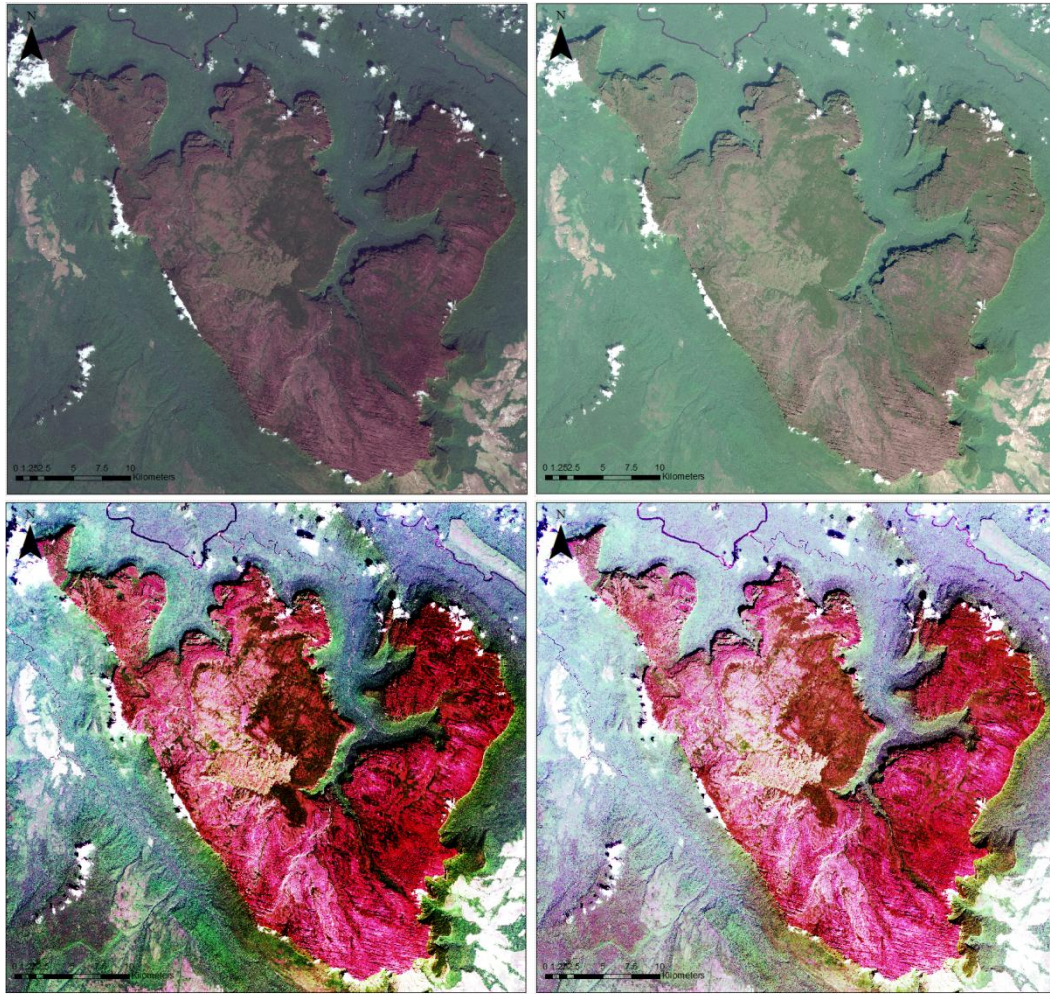
Figure 27. Natural Color Sentinel II image of Auyan Tepui, with four different types of contrast stretch applied. Clockwise, Non-stretched image, Standard deviation stretching, Histogram equalize stretching and Histogram specification stretching.

3.7 Processing of the points cloud

The last product is related to a rock wall crossed by some joints and located in the northern part of Auyan Tepui, close to one of the entrance of the Imawarì Cave entrance. The raw data is in the form of a point cloud, collected with a Laser Scanner device and characterized by a very high spatial resolution, since the point

48

density is of 1 surface point every 3 mm. A laser scanner is a measurement instrument able to automatically acquire spatial coordinates of a surface of an object, basing on emission and reception of a light beam. The scanner used is a Leica HDS7000, a phase difference scanner with 1.5 microns of wavelenght,1mm spatial resolution and flow rate of 187 m (Santagata et al., 2015; Sauro et al. 2016; data courtesy of Tommaso Santagata, La Venta esplorazioni geografiche e studio G.S.T. - Gruppo Servizi Topografici snc. di Geom. Camorani M.)

3.7.1 CloudCompare

The point cloud processing, has been developed with the open source software "CloudCompare", which is user-friendly and allows a large spectrum of analysis.

Firstly, the data has been uploaded in the software where, using the tool "Compute - normals", we calculated the vectors normal to the points: this computation is helpful to display the cloud, because it allows to enlarge the size of the points, in order to cover the empty spaces between them. Some parts o the cloud are missing, because in shadow with respect to the lidar light of flight.
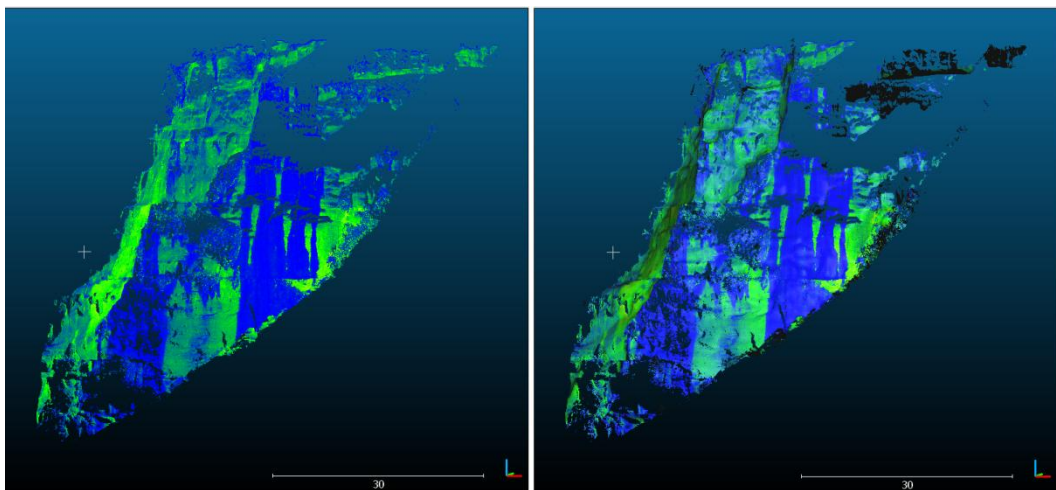
Figure 28: Point cloud appearance before (left) and after (right) the calculation of normals.

Once acquired, the point cloud lacks of geographical reference, which is, instead, of a crucial importance for the correct orientation of the structural features. For this reason, we firstly have assigned the north orientation to the point cloud, by knowing the correct location of the rock wall.

The North-direction has been geometrically inferred using a topographic map (scale 1:1000) of the area, and it results North - 340. Then, this value has to be applied to the cloud: with the tool "segment" we extrapolated a flat part of the surface, that approximate the overall orientation of the rock wall, and we calculated its best-fit plane. This plane, which has a default random orientation, has been oriented with the right angle to the north, applying a rotation matrix (Edit - Apply transformation), keeping the z-direction as a rotation axis: the rest of the cloud was adjusted accordingly.
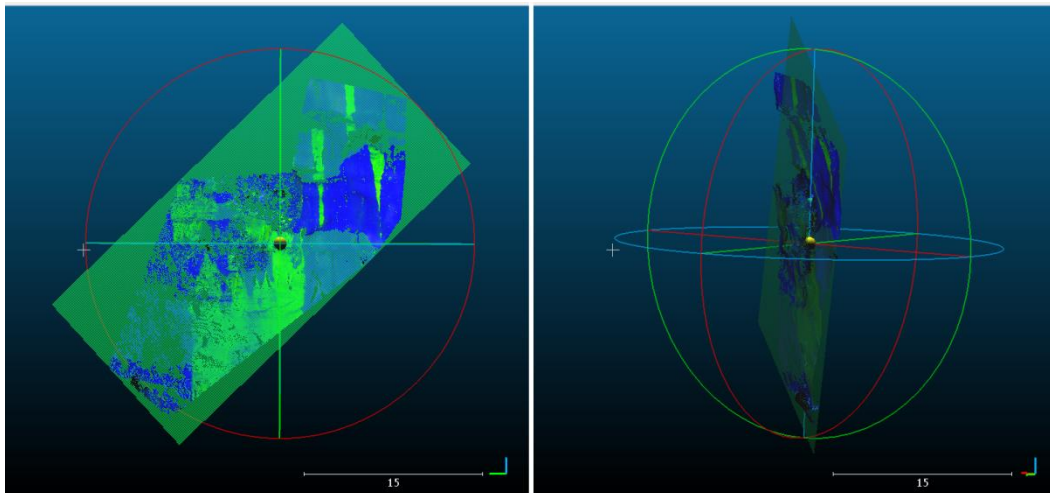
Figure 29. Segment of the wall surface and the calculated best-fit plane.

Howsoever, some errors are not excluded, due to the difficulty to the scale of the map and to choose a plane that represents in the best way the wall surface. A more precise georeferencing should be done using a triangulation of GPS points taken in various places on the surface, but this data are missing: the point cloud has not been georeferenced during the acquisition, and the outcrop can be reached only by organizing a new expedition.

3.7.2 Stereonet

Cloudcompare has a tool to compute and display stereograms, but with a lot of limitation, due to the fact that the program is not designed specifically for geology; by contrast, Stereonet allows several calculation and editing with different output formats, depending on our needs, on faulting or fracture data. The data obtained have been imported into Stereonet 9.5, to realize rose diagrams and stereoplots (these are reported in the chapter "structural analysis");
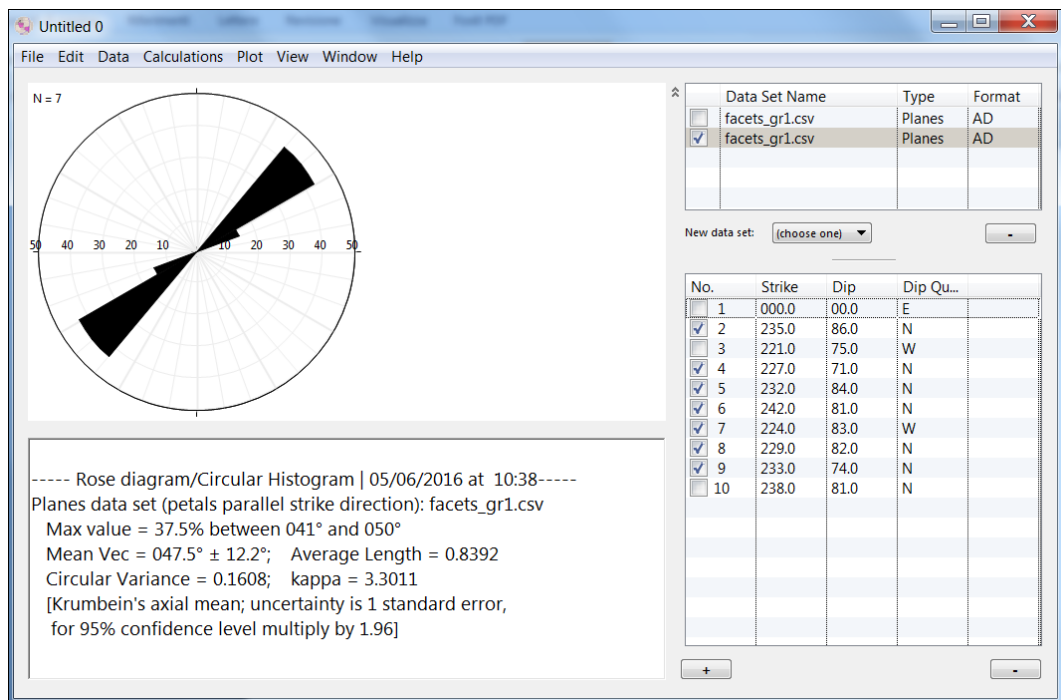

Figure 26. Example of Stereonet window.

4.Multispectral Image Interpretation

One of the intent of this work was to build, using remote sensing techniques, a geological map of Roraima Tepui and Chimantà Massif. The various features and lithological units have been recognized and mapped analyzing the Satellite images previously elaborated in ENVI.

The interpretation phase has been developed mainly using the software ArcGIS, database designed to store, process and analyze geographic data and geospatial information. The management of the files has been performed with ArcCatalog, while the visualization, analysis and editing is supported by the application ArcMap. Both the processed Sentinel II and Landsat 8 images were loaded in the data frame as raster files (as it is written in the previous chapters, the files have already been stacked, sharpened, resized ecc.), as well as the Aster G_DEM and all the thematic maps created The spatial reference of the satellite images are WGS_84 UTM_Zone_20N: the same coordinate system have been assigned to every file uploaded or created during the interpretation, in order to overlap the levels correctly.

The Aster G_dem files were merged into a single raster and then, using the hillshade tool, turned into a 3D representation of the surface. The image is shaded taken into account the sun's relative position, specified using altitude and azimuth properties. One of the most frequent errors using this tool occurs in setting the Z-factor: this parameter is used to adjust vertical and horizontal measurements into the same unit of measure (specifically, it is the number of vertical units in each horizontal unit), and is set to 1 by default. The z-factor is also influenced by latitude: a conversion table can be found in the Esri website: the study area is located between 5 and 6 degrees north; the relative value for the Z-factor is 0.00000912 meters. Not setting this parameter correctly makes the hillshades look heavy or leaden.
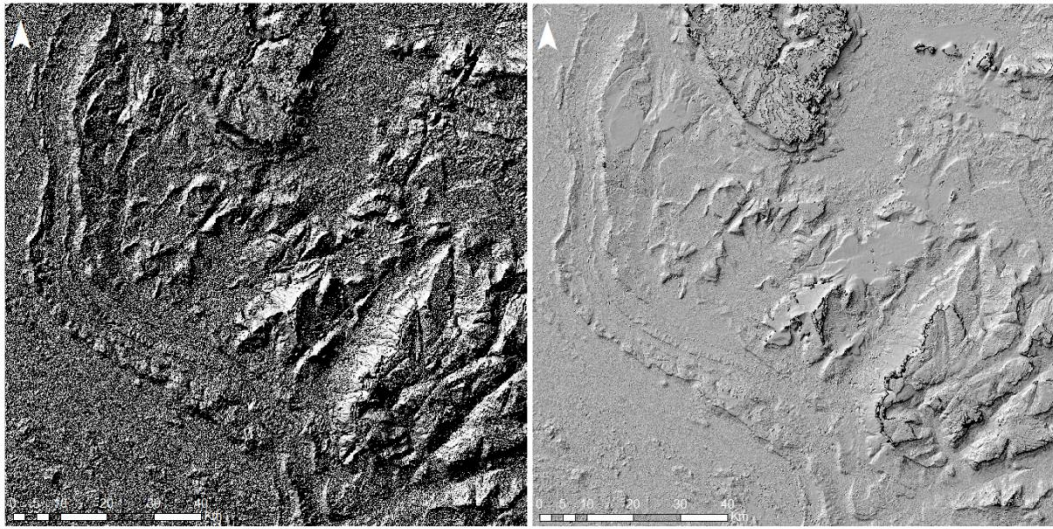
Figure 27. Left, a DEM where the Z factor was not chosen properly (without take in count the Latitude). This lead to a bad appearance of the image, that looks disturbed and with an irregular and rough aspect of the surface. On the right side, the same image processed in the correct way shows a smoother appearance.

4.1 Chimantà Massif

4.1.1 Mataui formation

As we know from literature, the upper part of the Chimantà massif, as well as that of the Auyan Tepui, is composed by massive quartzitic sandstone with low-grade metamorphic subarkoses, belonging to the Mataui formation. Observing the Landsat satellite image in "natural colors" the Mataui formation can be easily identified, as it constitutes the most part of the Chimantà surface: it appear brown-red in color, devoid of vegetation and with flat-shaped outcrops. It is crossed by an extensive network of joints and fractures which form a quite regular pattern, isolating several rhomboid rock prisms.

Figure 22. Landsat8 4-3-2 image of the Chimantà Massif, after the application of the Histogram Equalize stretching. Even with a quick look, it is possible to see the morphological difference between the two main domains that compose the surface: the sandstone and the diabase intrusions.

As it has been suggested by Prof. F.Sauro, the Mataui formation has been divided into two subunits, named "Upper Mataui" and "Lower Mataui", apparently separated by an unconformity. This can be inferred observing the Tepui scarp from aerial photos: as it may be noted, the summit plateau is often divided into two (or more) secondary platforms controlled by the layer surfaces, divided by a cliff of about 100-150m of height. Upper and lower sub-units, having the same petrographic characteristics, are undistinguishable by multispectral analysis.

The problem has been faced interpreting aerial pictures taken during the overflights of the tepui, which give a side view of the outcrop.


Figure 29. Lateral view of the Acopan Tepui, in the Chimantà Massif . Several plain surface are visible, located at different altitudes. (Archives la Venta - Theraphosa).

This approach is not possible everywhere, so the mapping has been carried out interpreting the various platforms located at different heights, as belonging to the upper or lower subunits. This may lead to errors in interpretation, since some of the surfaces can reasonably be formed along other different weakness layers within the rock body. It has been chosen to proceed carefully and opting for a conservative approach, mapping this difference just where it was more clear and pronounced.

4.1.2 Diabase Intrusions

Observing the Massif from aerial view, what it is catching the eye is that some areas of the plateau seems differ from the flat and regular sandstone: these bodies appear as low, rounded hills, partially covered by vegetation; differential erosion enhance this shape, affecting the landscape topography. Moreover, the regular fracturing network that pervades the Mataui formation seems to stop or, at least,

becomes less marked. These structures have been mentioned by Briceno (Briceno et. al., 1990) as subvolcanic bodies of Diabase composition; according to the author, Diabases crops out at different levels within the Mataui formation, with an upper organic-rich level of soil and locally presence of bauxitic material. They are probably the remnants of tabular sub-horizontal sills, intruded in concordance with the stratification of the quartzite.
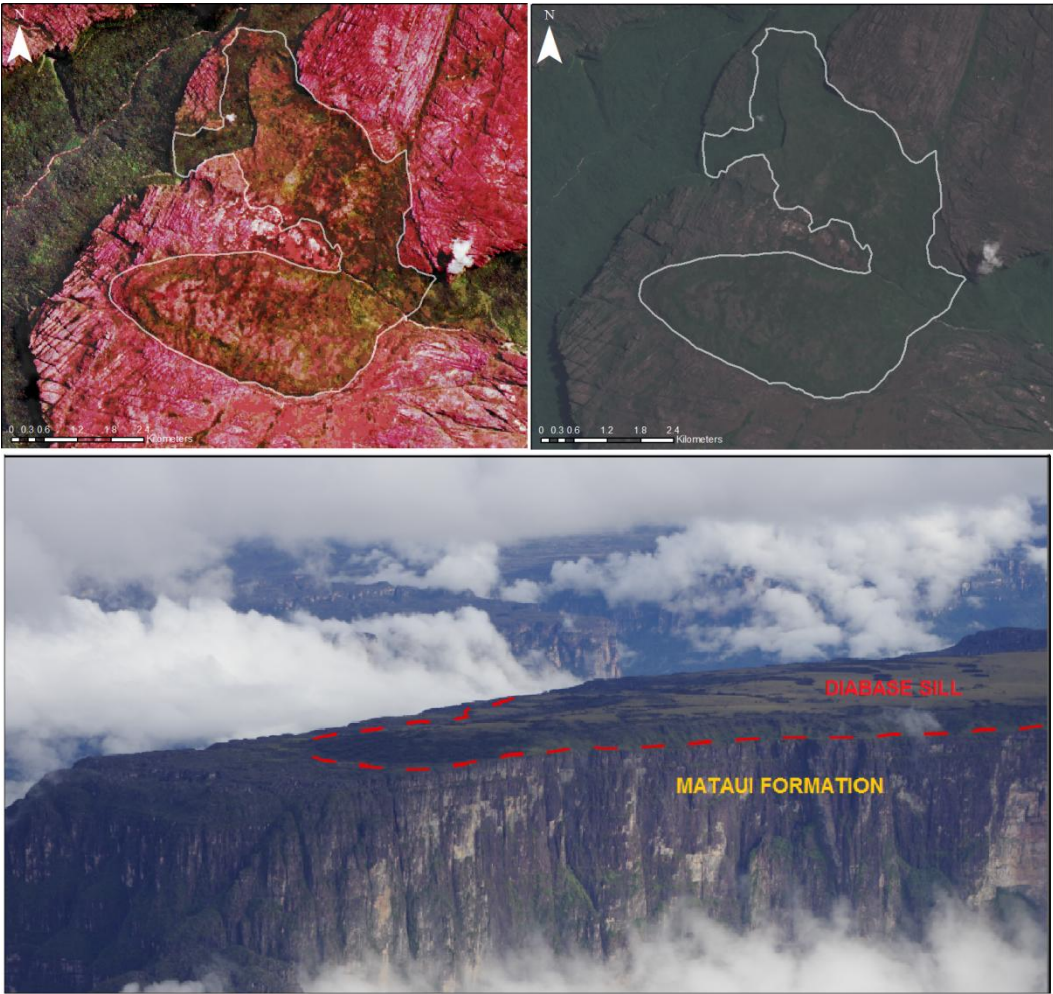
Figure 30. In the upper pictures: diabase intrusion represented in natural color, with Histogram equalize stretching (Left) and without stretching (right)The picture below represents a side view of the south-western edge of Acopan tepui (Chimantà Massif). The diabase lies down over the quartzite of Mataui formation. (Archives la Venta - Theraphosa).

4.1.3 Alteration zones

The intrusion of magma appears to be associated with the presence of alterations, emphasized in many images with different combinations of false colors (shown in the following picture). These phenomena may be related to the argillification of the volcanic mass, due to strong weathering or to the presence of hydrothermalism, subsequent to the intrusions, which may be the cause of the presence of other mineralizations. A useful method to ensure the existence of argillic alteration, is to verify the presence of clay minerals through the band rationing. The spectral bands used are N6 Landsat8 (SWIR I), divided for N7 (SWIR II). This particular combination allows to detect clay phyllosilicates as Kaolinite, Illite, Montmorillonite and Alunite (Sabins, 1996); the way to generate this type of image is explained in the previous section relative to the processing in ENVI.


Figure 31. Detail of the central part of the Chimantà Massif, with, edged with the grey line, the portions interpreted as alteration.

Observing the image below, it is possible to see that the weathering is pervasive along the entire surface of the diabase, which it is surrounded by alteration halos that may have hydrothermal origin. The quartzite areas more distal from the intrusive nucleus, looks almost undisturbed. In some places the intrusion seems elongated in the direction of the fracturing which, as we will see later, has been suggested to be subsequent to the intrusion of diabase: this may indicate that locally there are late magmatic events, with respect to the intrusion of the main body, dated 1.4-1.8 Ga (Briceño and Schubert, 1990; Santos et al., 2003).
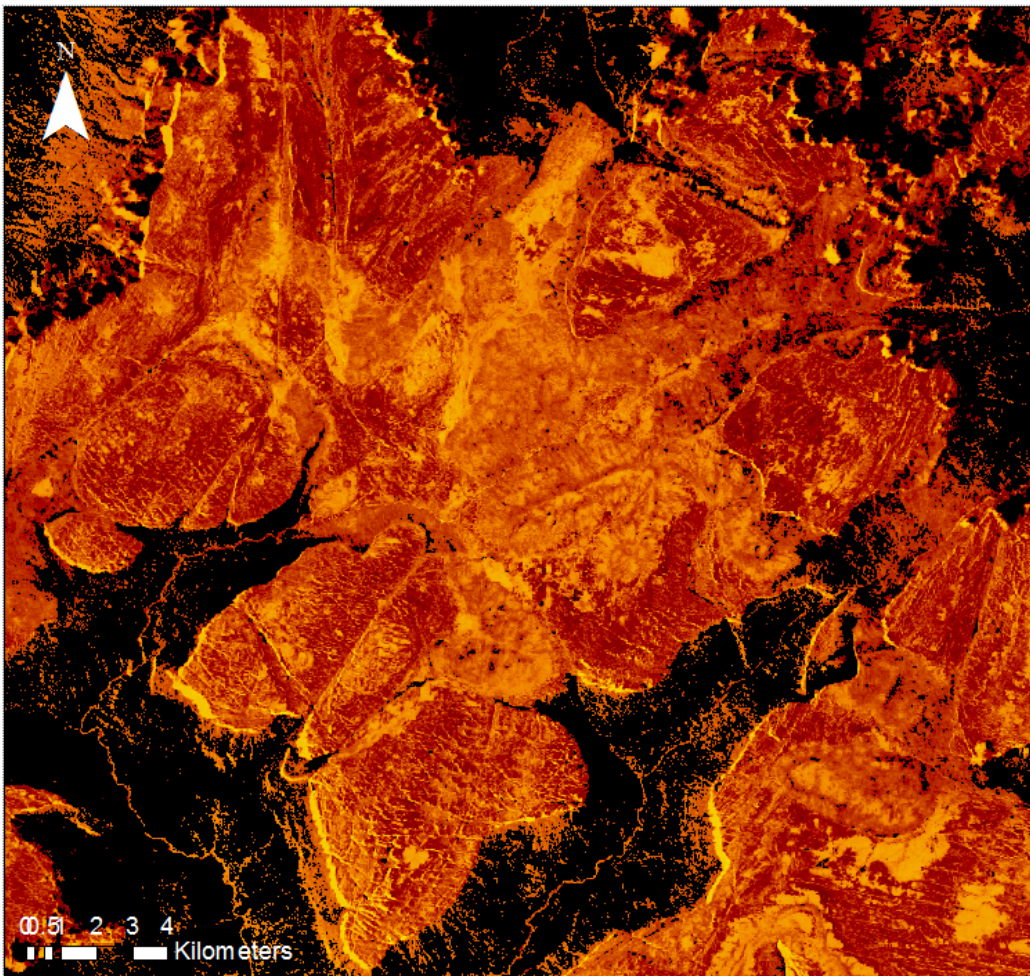
Figure 32. The result of the band rationing, performed on the Landsat 8 image of the Chimantà Massif, shows the presence of argillitic alteration; the presence of aluminum-phyllosilicates is represented with brighter tones.

Another help to distinguish the various components of the map comes from the use of the classification method. Firstly, we chose the combination bands that highlight better the various features, then, we created ROIs files for each category of elements discovered, which will be used from the software as the base to generate automatically the thematic map, following the maximum likelihood method . In this case, as a further evidence, we got a clear-cut distinction between the two main domains discussed so far, which make easier to draw the limits.
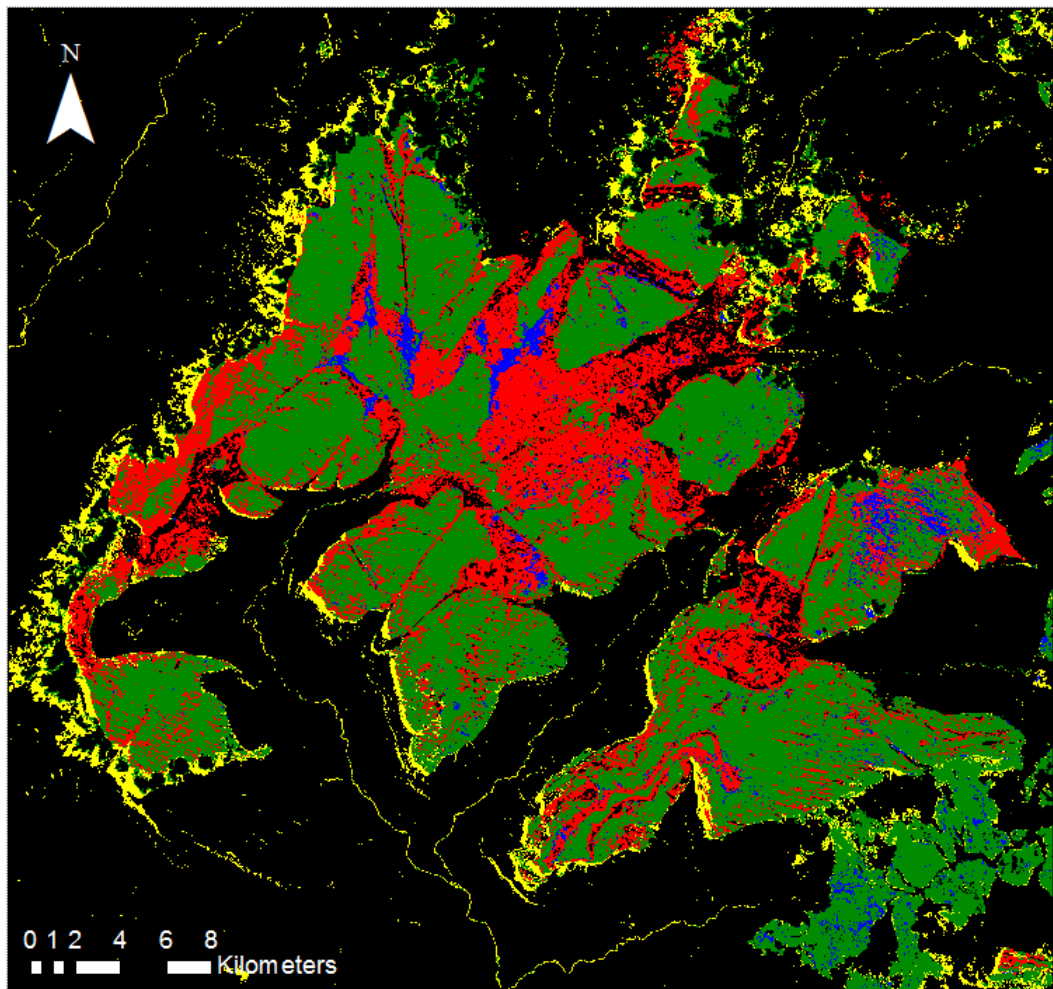

Figure 33. Thematic map created on the basis of a stretched Landsat 8 natural color image(4-3-2); black: masked vegetation and clouds; yellow (where not masked): vegetation; green: quartzite; red: diabase; blue: alteration.

However, this is not binding in order to edit our own map, but it turns out to be an excellent way to integrate and compare our visual interpretation.

4.2 Auyan Tepui

After the analysis of the Chimantà massif, our focus has been shifted to Auyan Tepui. As we know, Chimantà and Auyan tepui are remnants of a single plateau, and then basically consist of the same geological units.
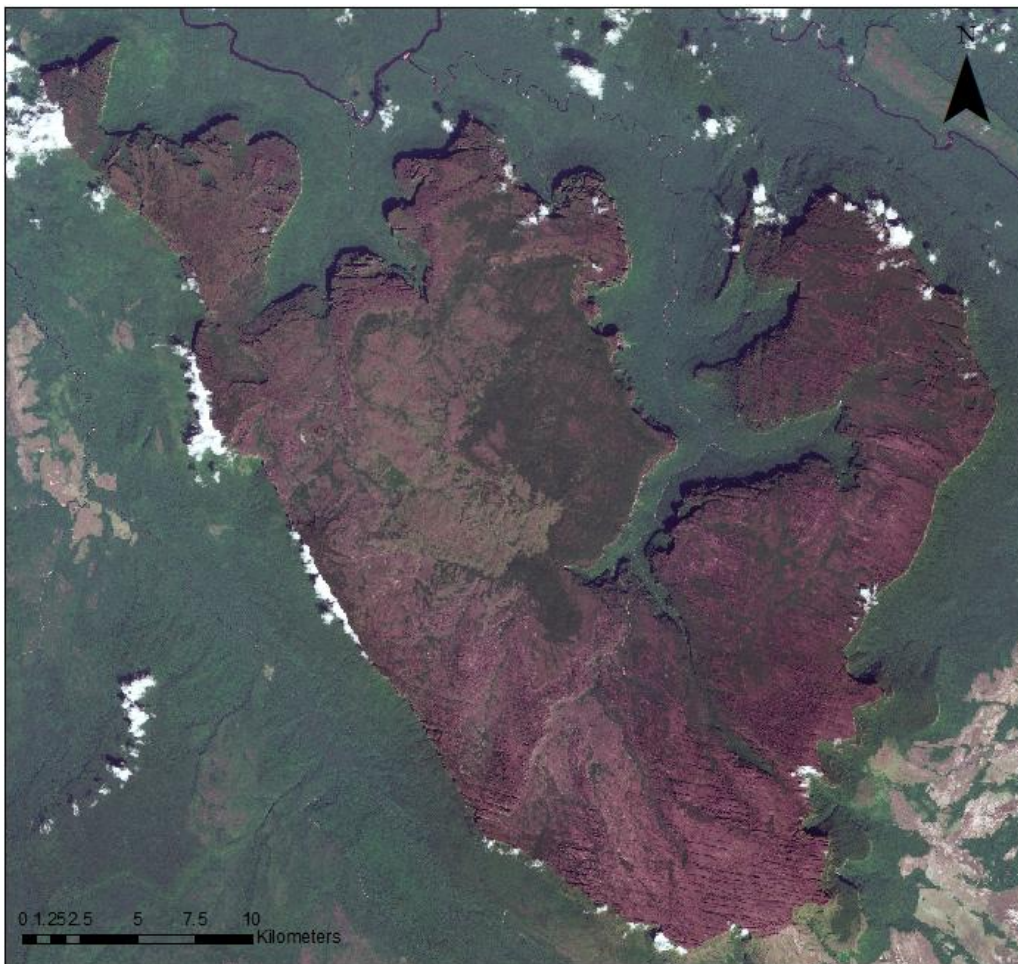
Figure 34. Sentinel II "natural color" (red, green and blue bands) image of the Auyan Tepui, with no stretching applied. Observing this image, it is possible to notice the similarity with some elements of Chimantà Massif, as the fracture

network and the presence of diabase, underlined by the presence of massive vegetation.

Since the Roraima group is slightly deformed, with broad fold that cross the area of study (Briceno 1982, Briceno and Shubert 1985), the thicknesses of the layers and the dip may differ. In this case, the analysis is based on a Sentinel II image, which have a better spatial resolution than the Landsat 8 image used for Chimantà.

4.2.1 Mataui formation

Similarly to the Chimantà Massif, the observation of the Auyan Tepui from satellite images points out that the Mataui formation occupy the majority of the plateau surface.

In line with our expectation, it show the same optical and geomorphologic characteristic, as a wide joint system and the absence of vegetation. Here, the division between upper and lower Mataui seems to be clearer, underlined by the presence of an inner scarp that divides the units.
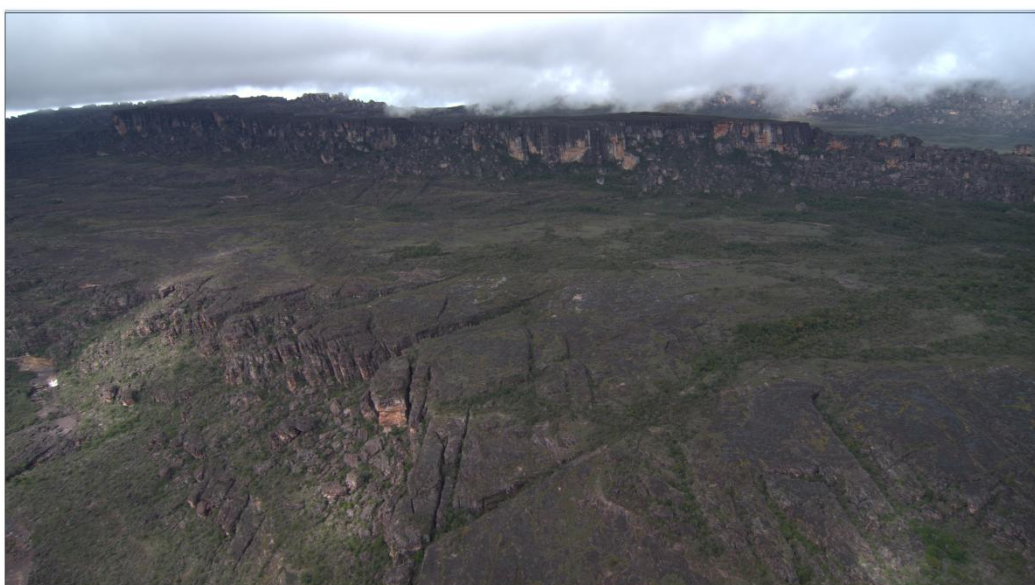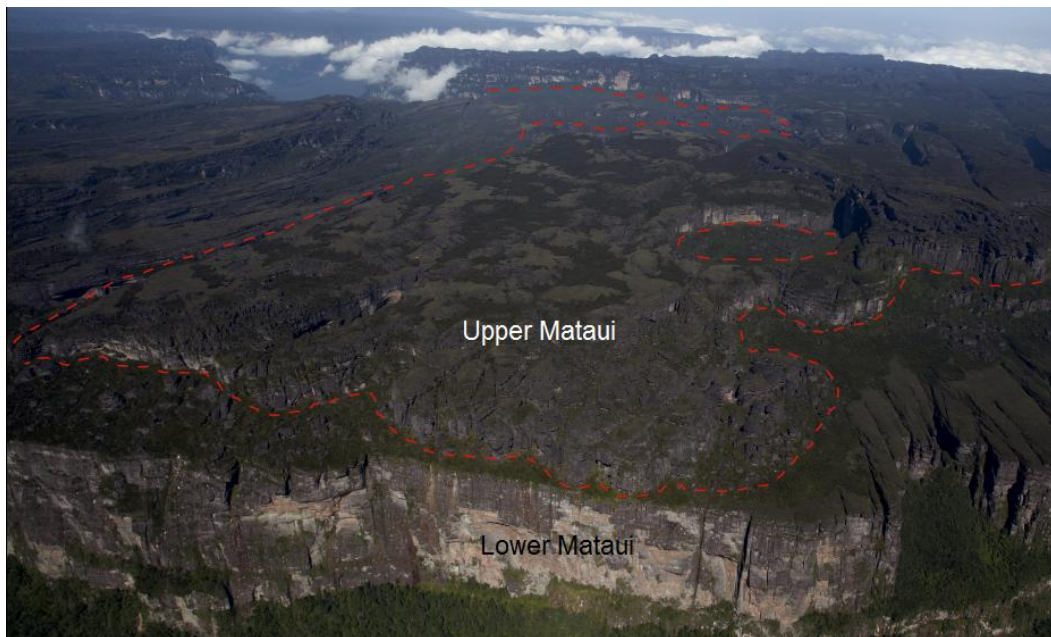
Figure 35/36. Aerial view of different parts of the Auyan Tepui, with the two main platform separated by an inner scarp. (Archives la Venta - Theraphosa).

In this case, the lower unit emerges on a much larger surface than on the tepui Chimantà, and forms the main body of the outcrop; the upper unit is significantly thinner, reasonably because of the millions of years of erosion to which has been subjected.

4.2.2 Diabase intrusion and alteration zones

As we previously seen, the ease in recognizing the diabase intrusion is mainly related to its vegetation cover. In this case we found a very large main intrusive body, located in the northwest area of the tepui (just above the head of the Angel Fall), and few minor spot elsewhere.

Contrary to what happens on Chimantá, The distribution of diabase does not seem to follow specific directions, and it appear as remnant of a single-event sill intrusion. Observed from the aerial photographs given by F.Sauro, it can be seen that morphologically they appear as rounded vegetated hills, resting on the flat surface of the Mataui Formation.

62

Figure 37. Auyan Tepui: Smooth and rounded hills formed by the erosion of the diabase sill, extended over the quartzitic sequence of the Mataui formation (Archives la Venta - Theraphosa).

By changing the combination of bands and the contrast stretching, the difference between lithologies results accentuated. In particular, it is detected the presence of a large zone of alteration associated with the diabase, which cover a wide area in the inner part of the plateau and shows a sharp and well defined boundary with the quartzite.

Further confirmation comes from the file created by the division between bands; in this case they are, respectively, B8 (0.842 µm) / B12 (2.19 µm) of the Sentinel II image. Observing it, the distribution of aluminiferous phyllosilicates (Kaolinite, Montmorillonite ecc.) well match with the area that we have classified as alteration.

Also in this case, the use of the classifications method is of a great help to categorize and map the various features of the area. It clearly separate the diabase (represented with red color) from the alteration zone (green); upper and lower Mataui are shown in blue.
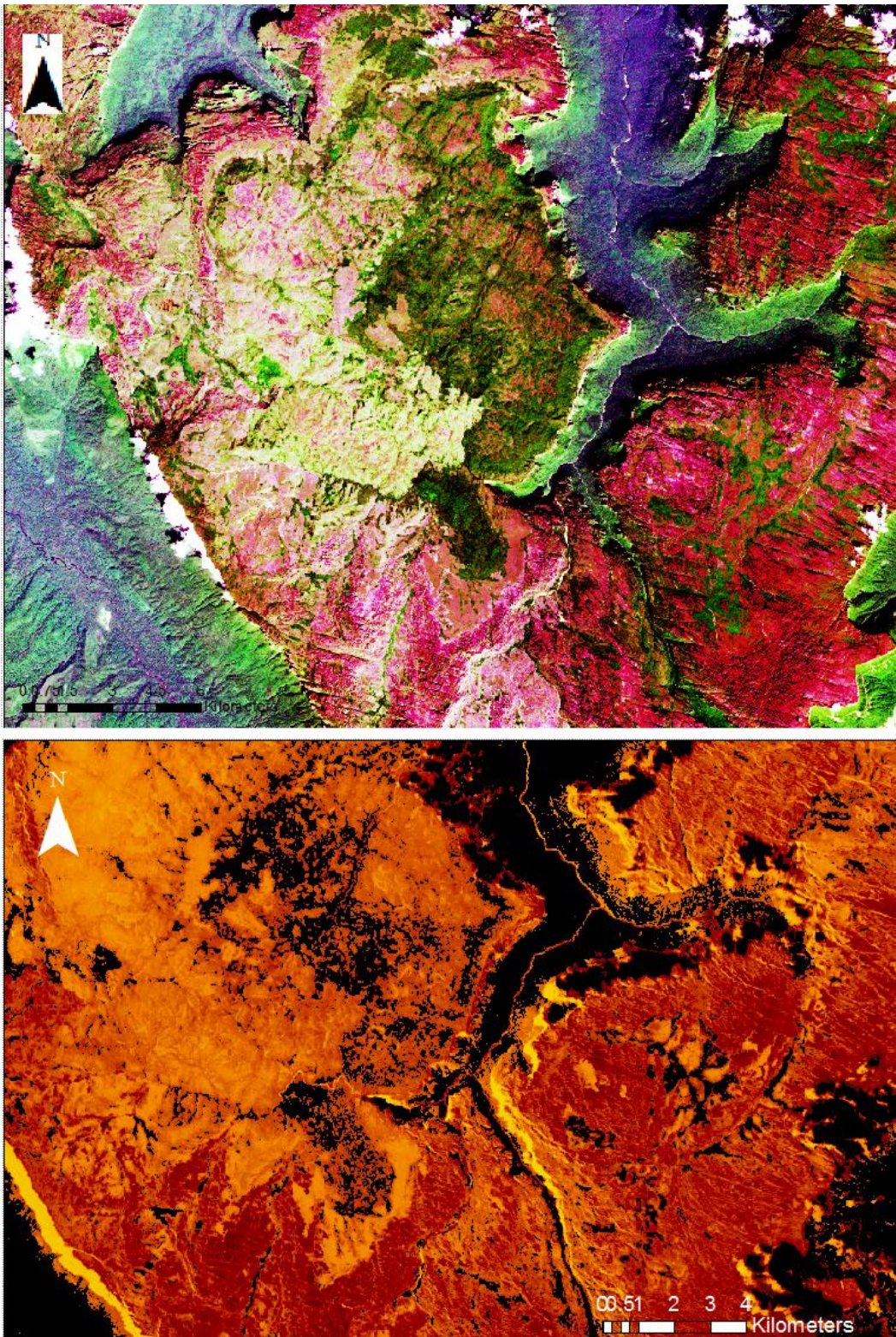
Figure 38/39. Sentinel II (3-4-1 bands combination) image of the Auyan Tepui diabase and alteration. The picture below reveals the presence of argillification:

*clay minerals are highlighted by bright tones.*
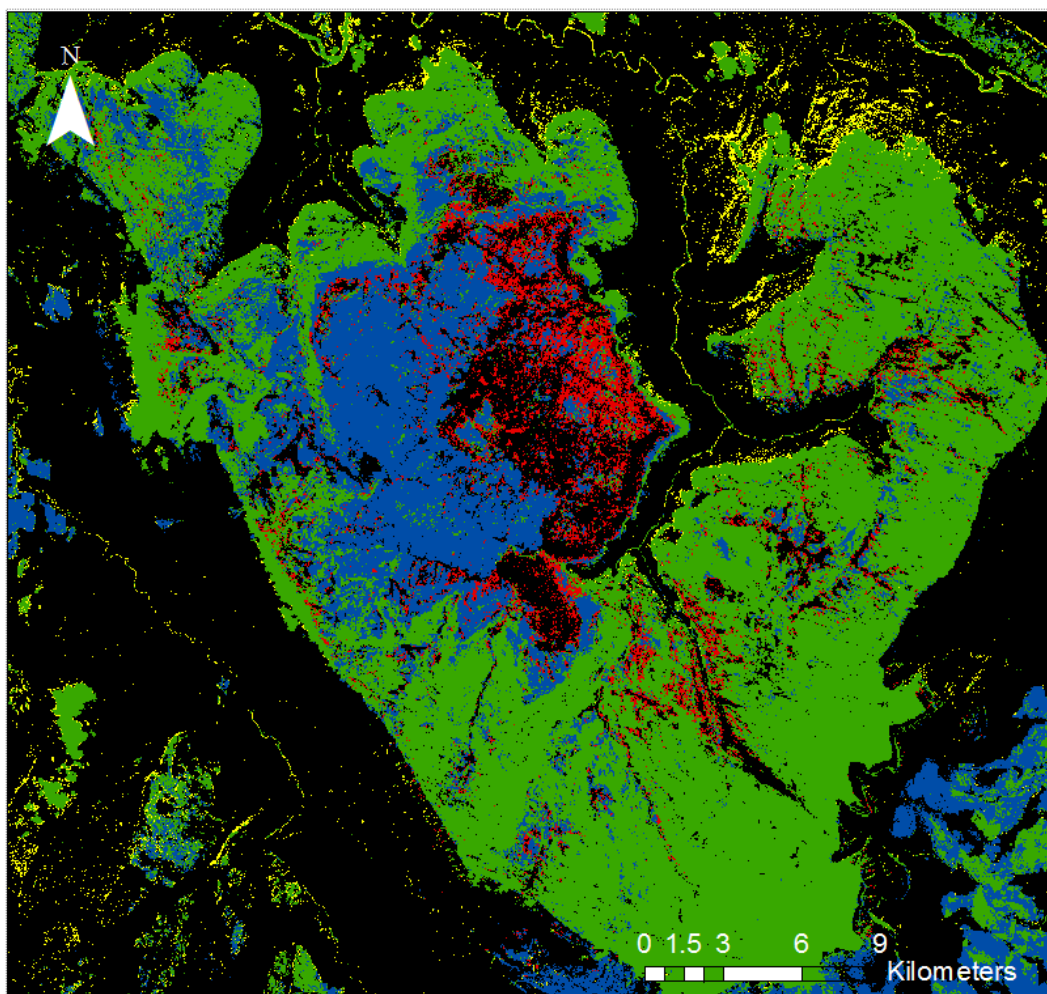
Figure 40. Thematic map created using a stretched natural color image(3-2-1); black: masked vegetation and clouds; yellow (where not masked): vegetation; green: quartzite; red: diabase; blue: alteration.

4.2.3 Uamaipué formation

Following the mapping of the summit of the Tepuis, we tried to recognize the units along the slopes at the base of the cliffs that surrounds these mountains. In this case, the environment is dominated by the lush vegetation typical of these latitudes, and this reflects in the scarcity or lack of outcrops. This fact made the

attempt very difficult to carry on; therefore, the problem has been faced from a geomorphologic point of view, through the use of the DEM and some photographs. Essentially this part is based on the recognition of the presence of ledges and walls (typical of the outcrops of a sedimentary sequence), visible thanks to the Digital Elevation Model, otherwise hidden by vegetation. According to Reid (1974), the outcropping sequence between the base of the tepui and the lowlands surface, belongs to the heterogenic Uamaipuè formation, which is made of made of proto-quartzites, arkoses and graywackes, with beds of cherts, lutites and siltites.
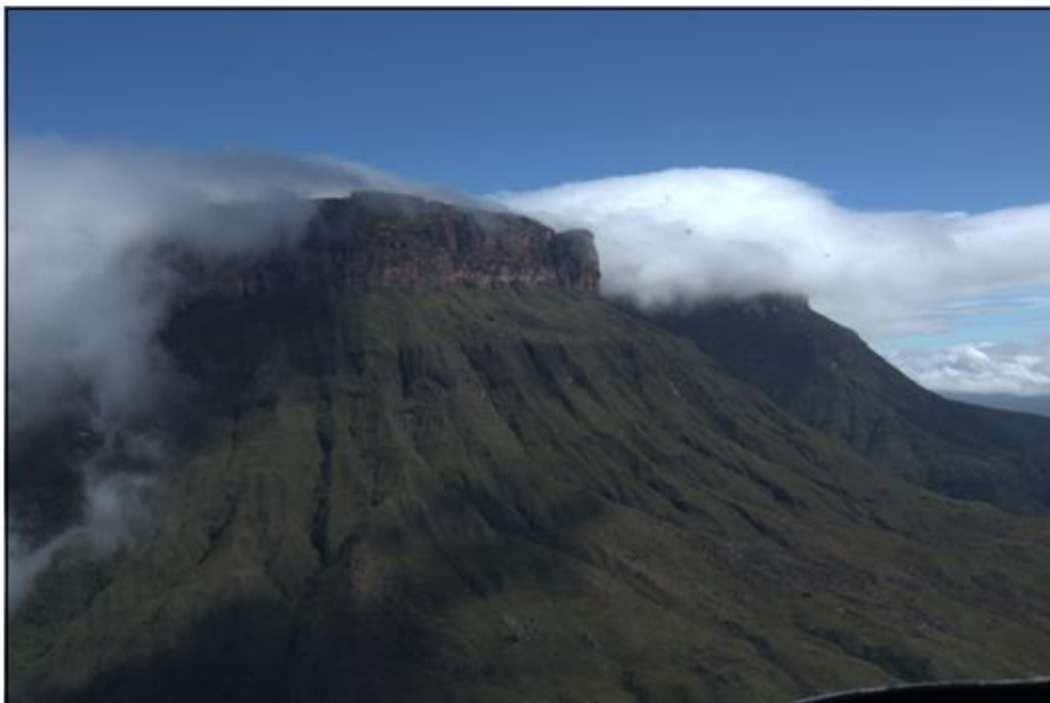
Figure 41: Foothill of Auyan Tepui (Archives la Venta - Theraphosa).

5. Structural Analysis

5.1 Introduction

The Tepuis area is part of the larger Guyana shield, which in turn represents the northern portion of the broader domain of the Amazon Craton. By definition, a craton is an old, stable and thickened part of the continental lithosphere, generally found in the interiors of tectonic plates, without recent tectonic activity.

However, the presence of various tectonic features in the area of study is unequivocal: the last part of this thesis is concerned to provide a description and analysis of the deformation structures and hopefully to suggest a likely origin. Unfortunately, the literature regarding this topic is poor, and the few information that I found, come from the works of Briceno (1982) and Briceno and Shubert (1985). According to the authors, the table mountain area has been slightly deformed, with large-scale syncline and anticline folds with about N/S and NW/SE trending axes.

The west limb of a syncline fold is visible in the westernmost portion of our study area, where a series of homoclinal reliefs emerges from the lowland, forming hogback structures; this series of long and narrow ridges and steep slopes has eastward/north-eastward dip. This structure can be appreciated observing the ASTER elevation model (following figure) or through the Landsat images freely available on Google Earth. It is clearly show how this type of tectonic structures has a strong influence on the morphology and hydrology of the area: the river Caronì (the second most important of Venezuela and main tributary of the Orinoco river) flows for part of his length, in the valley between the two crests. Nearby the study area, others gentle synclinal structures emerge from the Gran Sabana lowland; some of them are visible on the geologic map of Venezuela, e.g. the Cerro Aradan area, located west of the Caronì river.
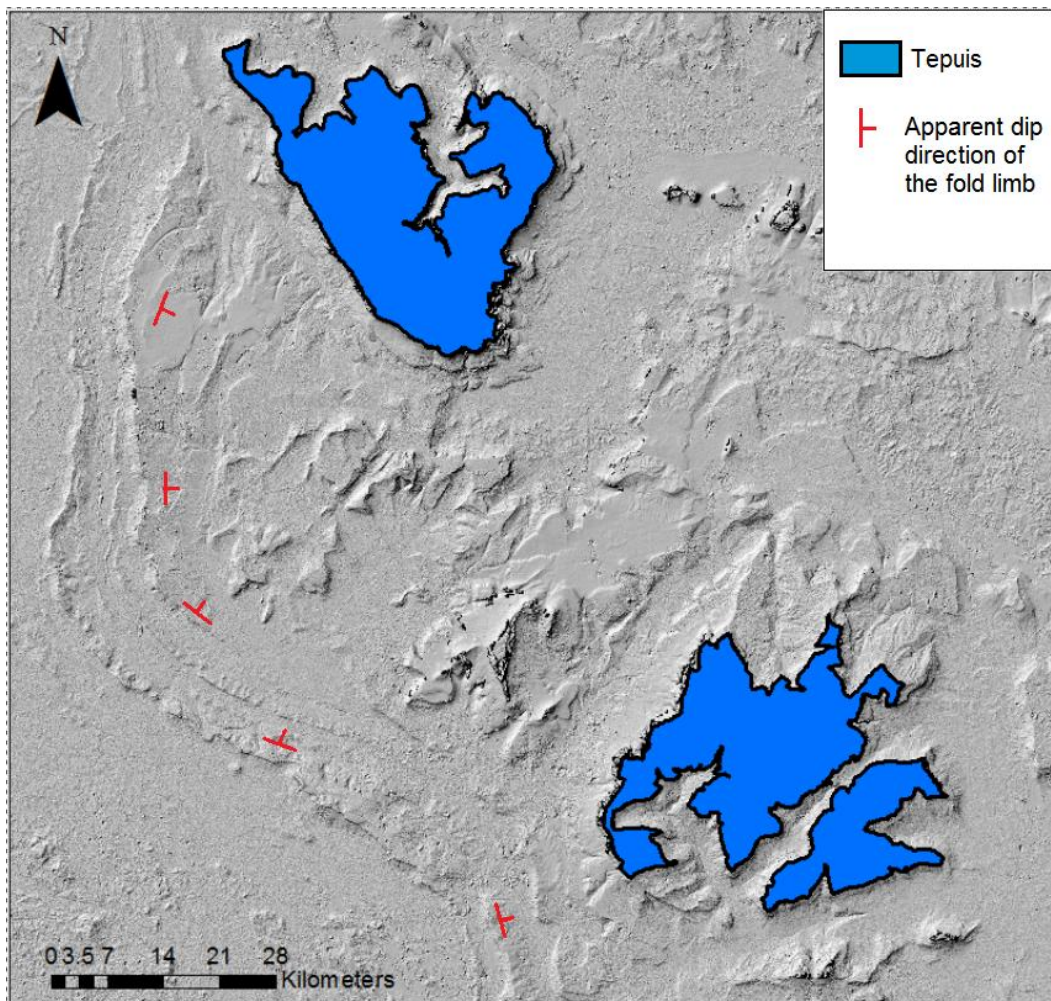
Figure 42. Limb of the fold emerging from the lowland, visible from ASTER G_DEM image.

5.2 Regional scale fracturing

From the study of the satellite images, the Mataui formation of both the Tepuis seems to be affected by abundant high angle fracturing. Focusing on the Chimantà Massif, the fractures detected have been grouped in two different classes, basing on their morphological characteristics: the first class, which is also the most representative feature characterizing the plateau, consists in two sets of straight joint, normal to the bedding, that cover the entire surface of the massif; they show

a regular spacing and intersect with a constant angle, creating a particular network of rhomboid prisms.
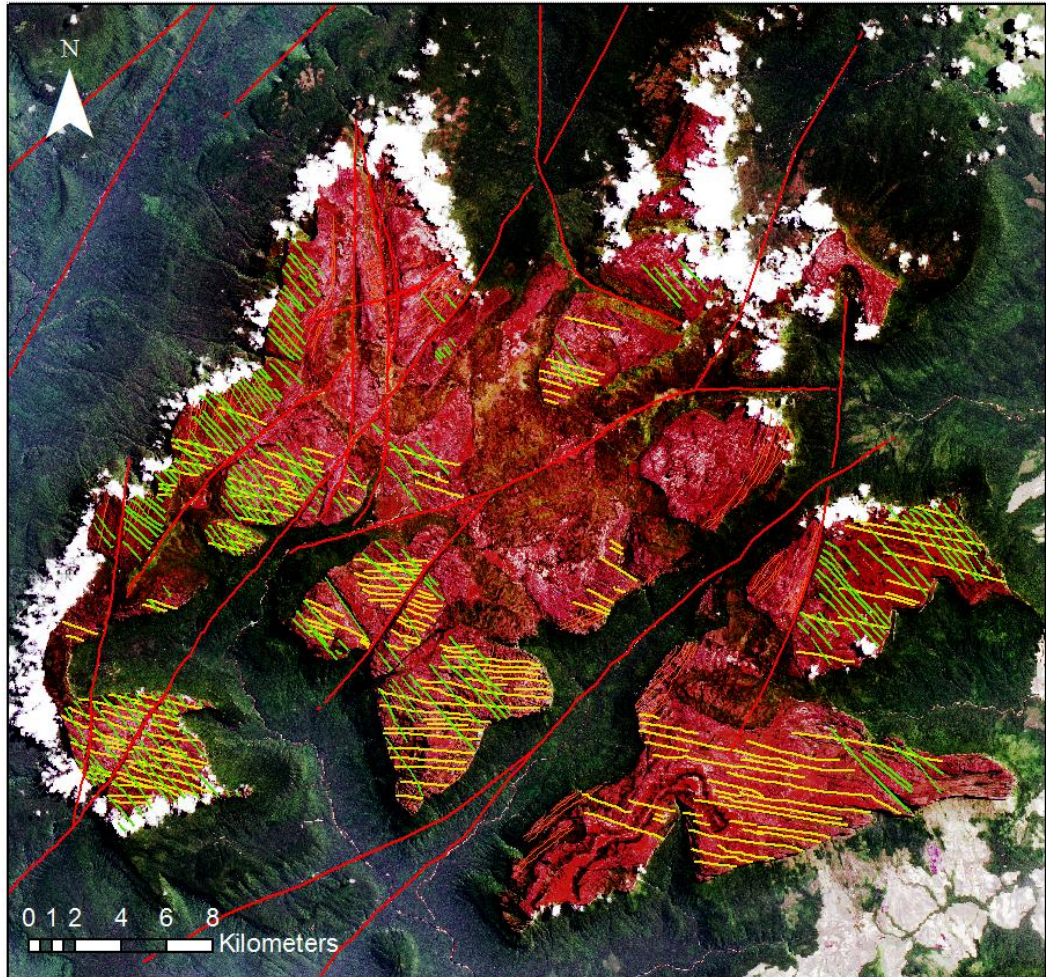
Figure 43. 4-3-2 Landsat 8 stretched image of the Chimantà Massif, with the 2 sets of conjugate joints (represented in green-yellow colors) and the major fractures (red).

The other group includes major fractures with tenth of kilometers of extension and various orientation (mostly NE/SO, and, less frequently N/S), which appear strongly eroded and forms deep and narrow canyon that cross the Tepui surface. Analyzing the Digital Elevation Model, it has been discovered that fractures of this type are also present in the surrounding lowland. No evidence of displacement has been observed in both the classes of fractures. Locally, a third

set of joints has been found, specifically in Apacarà Tepui and on the margins of Toronò and Acopan Tepui.
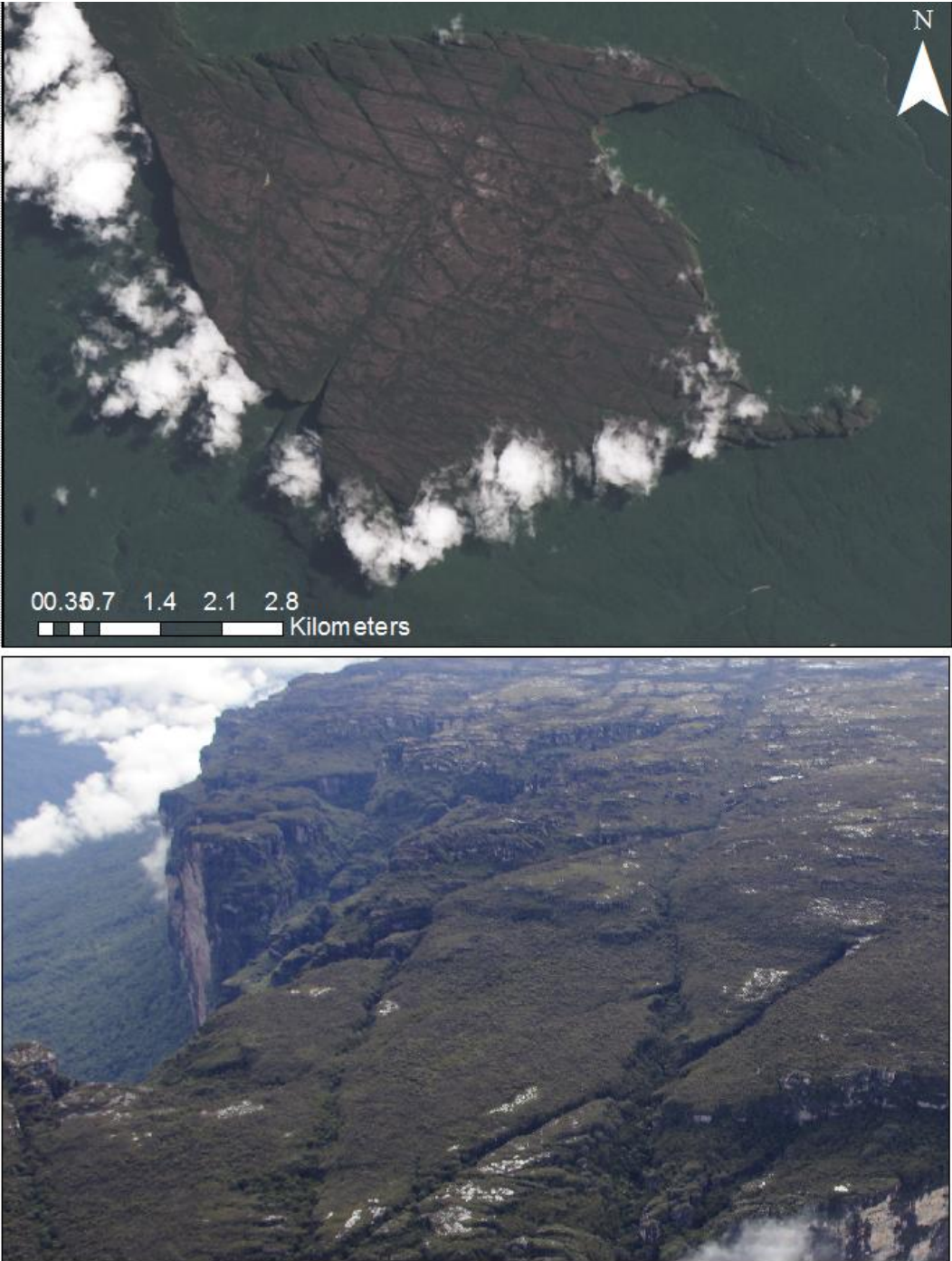
Figure 44. Fracturing in Abacapà Tepui (Chimantà Massif), and detail of a rhomboid rock prism formed by the joint network. (La Venta - Theraphosa).

They form areas with high-density of fracture, in correspondence of some of the main lineaments. In this case the joints are less pronounced, parallel to each other and elongated in the same direction of the main NE/SW fractures, with which they may constitute a single deformation zone. The presence of the fracture network on the diabase surface has been matter of discussion: at a first glance, the various tectonic features that cross the Mataui formation seem to be interrupted by the intrusion.
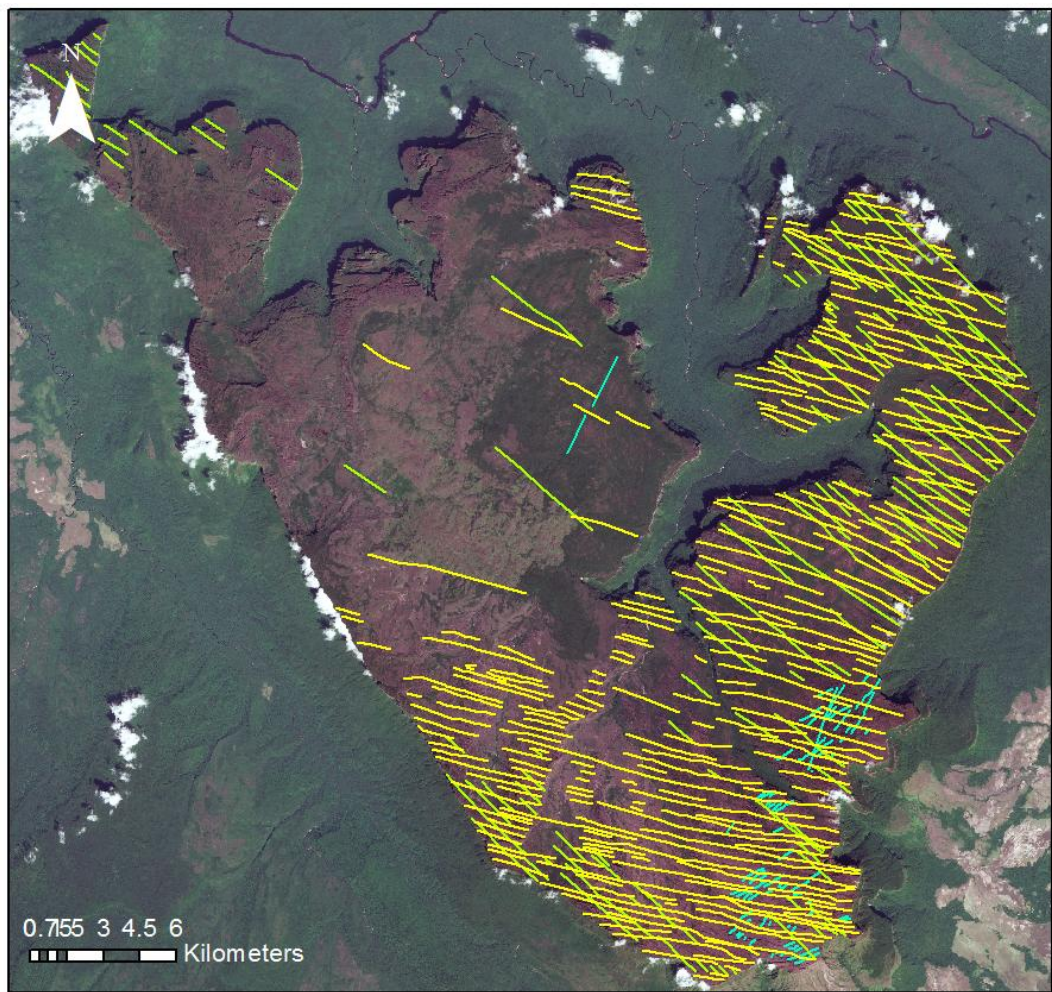
Figure 45. Fracturing in Auyan Tepui: the main joint system is represented in yellow and green, minor joints in blue.

A closer look shows that the diabase is actually crossed by some of the fractures: only few of them are clearly visible, and this may be a consequence of the high presence of vegetation and soil, which hide and smooth the shapes.

However, the presence of fracturing in the sub-volcanic body is of a primary importance, since it allows us to place the tectonic event subsequently to the Proterozoic intrusion event .The study carried out on Auyan tepui shows a slightly different situation: in this case the outcrop seems not affected by the presence of major fractures; instead, the surface is characterized by a network formed by two crossed sets of vertical joints, similar to the pattern found on Chimantà. Minor joints have been found locally: these are often smaller and confined between two parallel fractures (see image below) with an average NNE trend direction.

*Figure 46. Detail of the Auyan surface with the pervasive fracturing.*

On the Auyan Tepui surface, the presence of fracturing within the intrusion has been ensured using a convolution matrix, to emphasize the presence of edges and straight segments (the method is explained in the chapter 3.5)
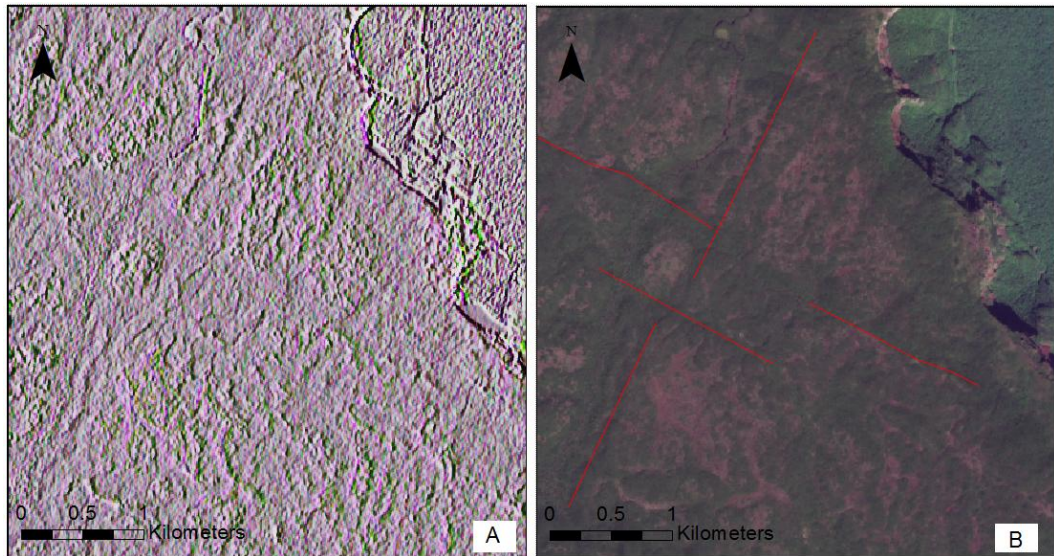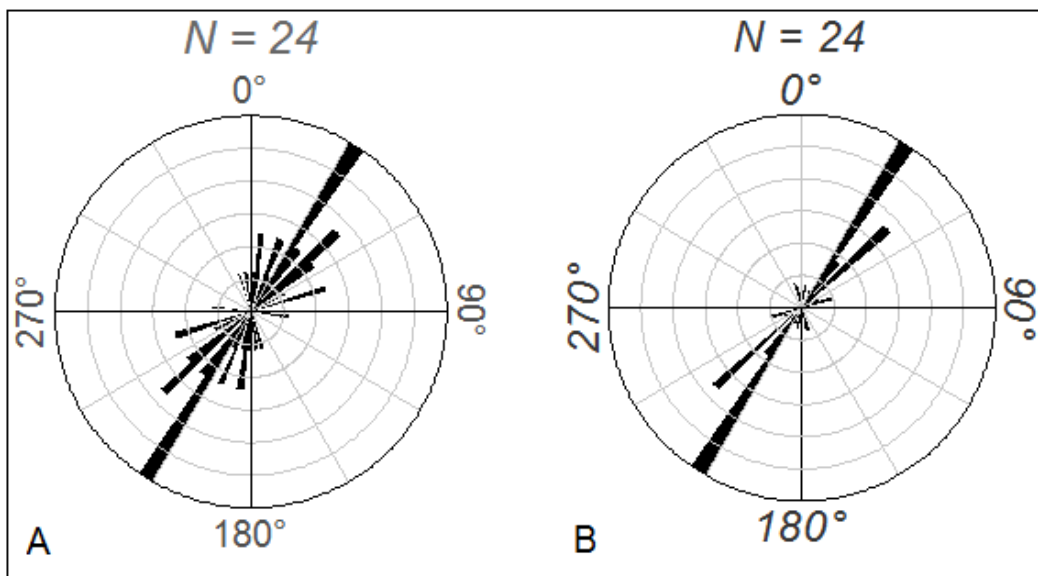

Figure 47. The presence of fractures in the diabase intrusion has been ensured applying a directional enhancement convolution matrix: in the picture A is represented a portion of the diabase surface with the directional edge enhancement applied, while in the figure B the same area in represented in natural colors,

5.2.1 Results

To represent the fracture systems, we have created polyline shapefile and we traced the lines following the joints direction. Using the GIS plug-in "polar plot v.1.0.250. developed by Jennes Enterprises", the various fracture orientation have been represented through rose diagrams.
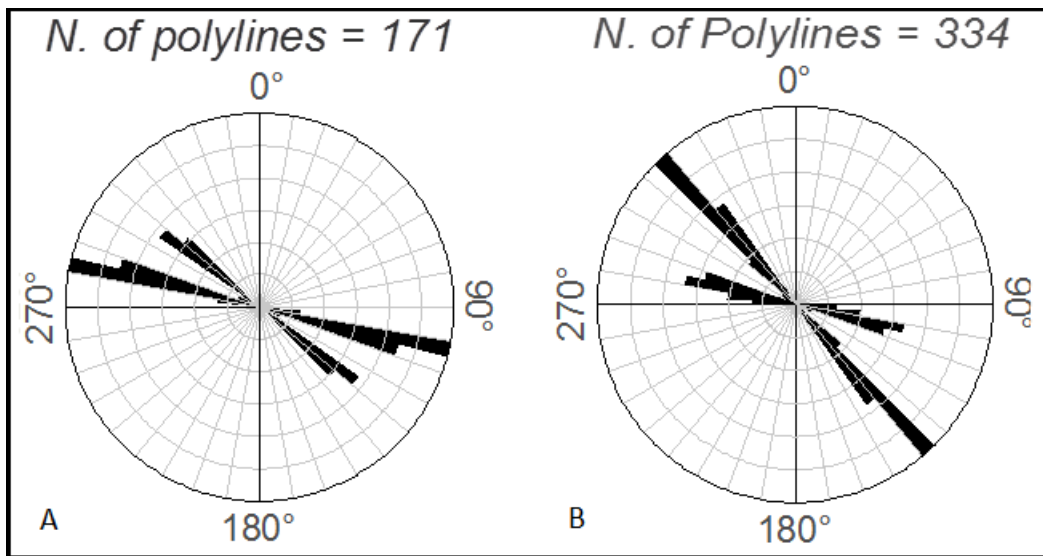
Figure48: A) Rose diagrams of the joint networks of A) Auyan Tepui and B) Chimantà massif. (Number of polylines = number of fracture included in the diagram)

Figure 49: Rose diagrams of the main fractures: A) not weighted; B Weighted by fracture length. The presence of a main direction of fracture is even more accentuated taking into account the fracture length.

74

5.3 Small scale fracturing

The information collected about regional-scale fractures were integrated and compared with new small-scale data, derived from the analysis of the point cloud, representing an outcrop located in the northern part of Auyan Tepui, in proximity of one of the entrances of the Imawarì-Yeuta Cave.
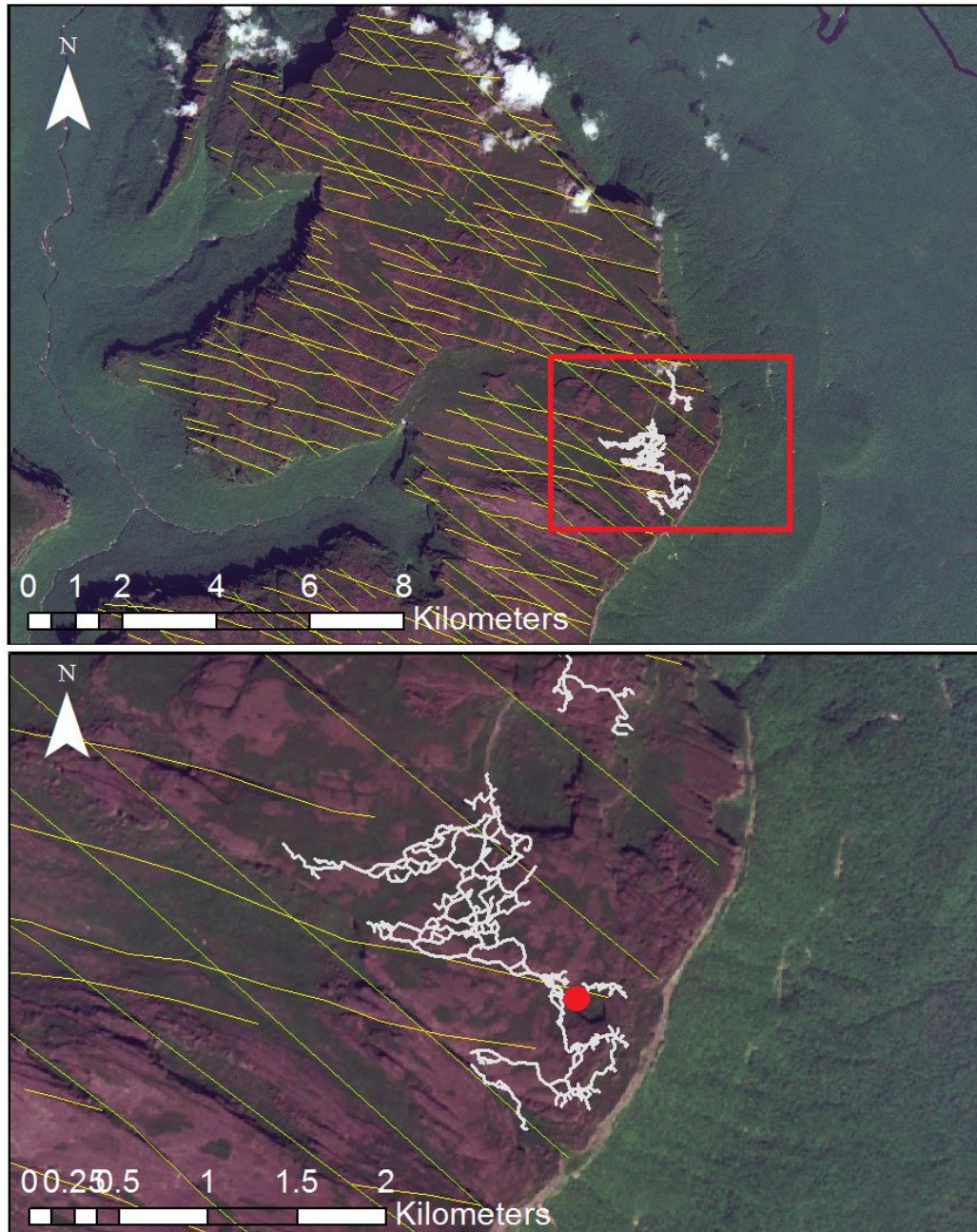

Figure 50. Fracturing in the northern part of Auyan Tepui, and location of the

The outcrop consists in a quartz-arenite rock wall, belonging to the Mataui formation with NNO orientation, crossed by multiple sets of fractures. From the point cloud we have cut out the zones where the fracture planes are present and more evident. Using qFacets Plugin (developed by Thomas Dewez, BRGM), it is possible to automatically detect and extrapolate planar surface from the cloud: the K-d tree algorithm divide the cloud in small planar patches (group of few surface point), which are then fused in bigger facets.

In the K-d tree dialog window, it is possible to set some important parameters, used by the software to conduct the fusion process, such as the minimum number of point per patch (we left the default value of 10: this means that patch smaller than this value are discarded), the maximum angle between neighbor patches and maximum distance between the merged patches and the current facet center.
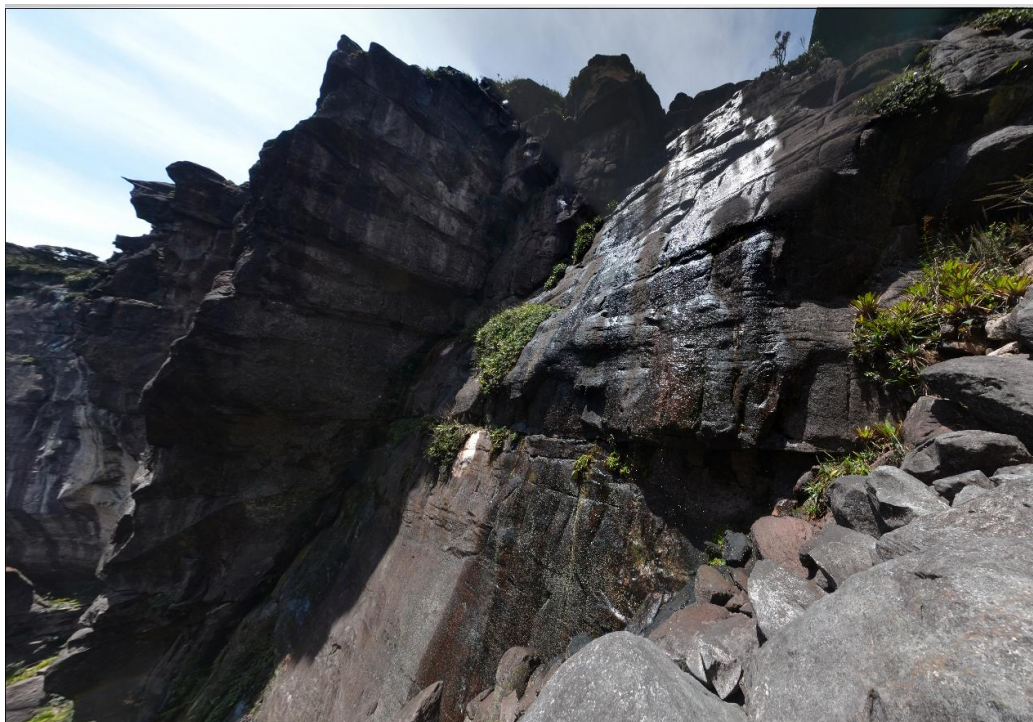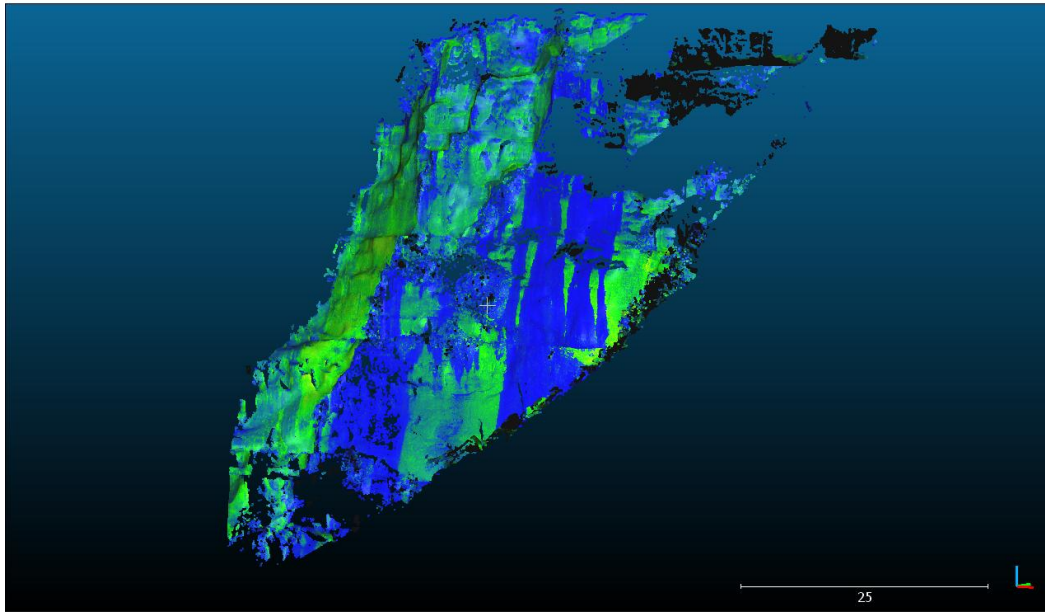
Figure 51/52. Previous page: Picture of the studied rock wall taken by the position Laser Scanner device. The Same outcrop is represented in the image above, by point cloud. (La Venta - Theraphosa).

In output, the software displays a complex texture composed by all the identified surfaces, grouped by color on the base of their spatial orientation. Once we get the facets framework, those that fit our fracture surfaces have to be detected and separated from the rest: to ensure not to chose the wrong ones, the facets file and the points cloud file have been overlapped to verify the matching between facets and correspondent surfaces.

Specifically, we picked out all the planes that we suppose to belong to the same group, on the base of their similar orientation: the selection can be done both from the catalog tree or from the workspace, clicking on the element, and saving it in a new folder. As a result, we identified three series of facets representing our fractures, and one, which represents the bedding planes (horizontal).
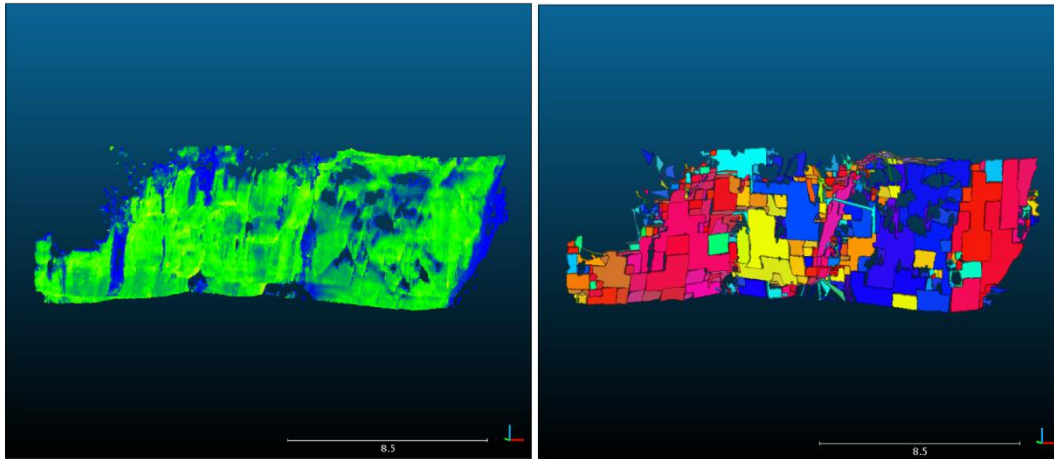
Figure 53. Detail of the point cloud and the plane surfaces detected by the qFacets plugin. Facets are represented in different colors, according to their orientation (they have been grouped in sets with a range of 5 degrees).

Every facet is associated to its spatial information (i.e. dip, dip direction; automatically calculated by the program) that we need to extrapolate and make available for analysis in other softwares. In this sense, the qFacets Plugin turns out to be useful, since it has a specific tool to export various information on a set of facets, in different formats (e.g. ASCII, shapefile).
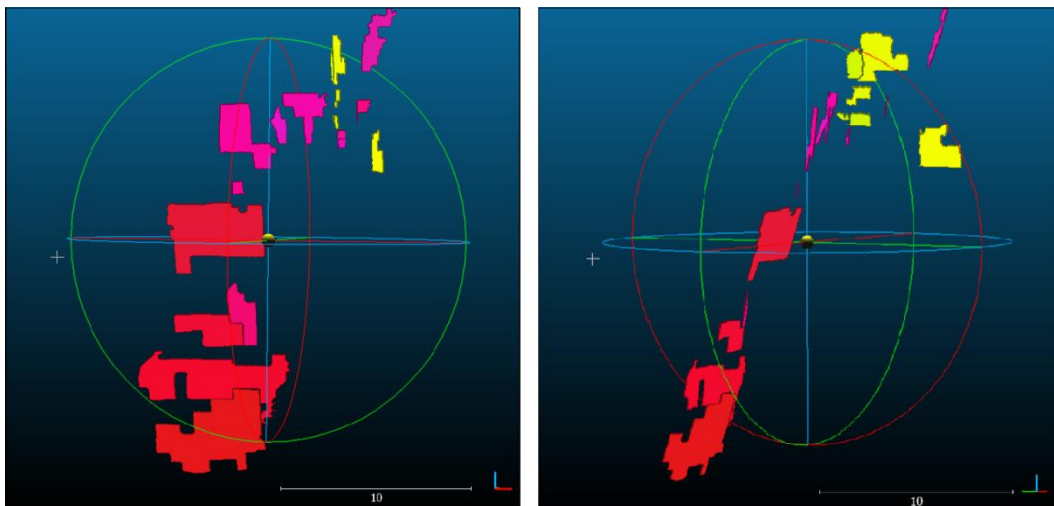
Figure 54. Detail of the facet extraction and relative position of the 3 systems: group1 (purple), group2 (red) and group 3 (yellow). The views are from 2 different angles.

5.3.1 Results

We have collected data relative to 16 fracture surfaces, divided into 3 groups according to their similar strike: they have, on average, these orientation: N 231°; N155°; N262°. The collected data are reported below. As for the regional-scale fractures, the joints orientation have been plotted on a stereoplot, group by group and all together, using the software Stereonet: the results are shown both as planes and rose diagrams. In all the three groups, the fracture show an almost vertical deep, which range between 71° and 89°.

Bedding planes: facets detected: 5; average dip: 4°

bedding	dip	dip direction	strike
1	0	0	0
2	9	157	247
3	1	197	287
4	5	316	46
5	7	272	2

Group 1: Facets detected: 7; average strike: N 231°; average dip: 80°;

Group 1	dip	dip direction	strike
1	86	325	235
2	71	317	227
3	84	322	232
4	83	314	224
5	82	319	229
6	74	323	233
7	81	328	238
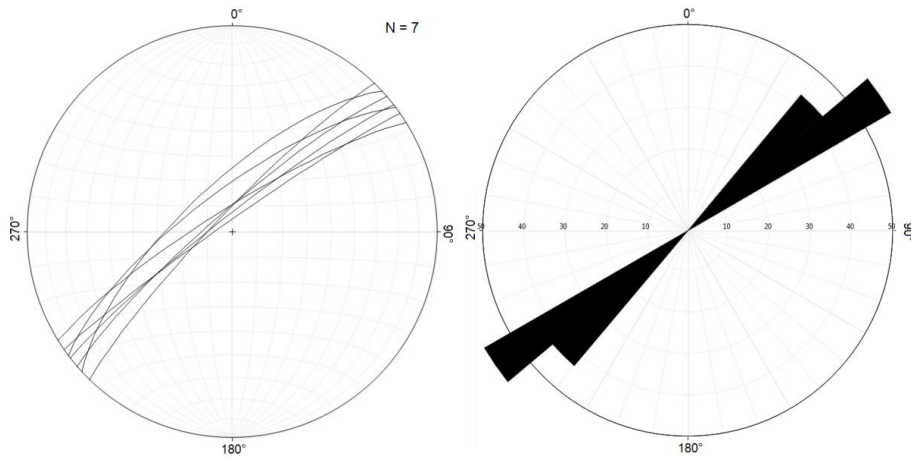
Figura 55. Stereoplot and rose diagram of the first set of joints.

Group 2: Facets detected: 5; average strike: N 155°; average dip: 87°.

Group 2	dip	dip direction	strike
1	87	65	155
2	85	70	160
3	88	63	153
4	89	62	152
5	86	69	159
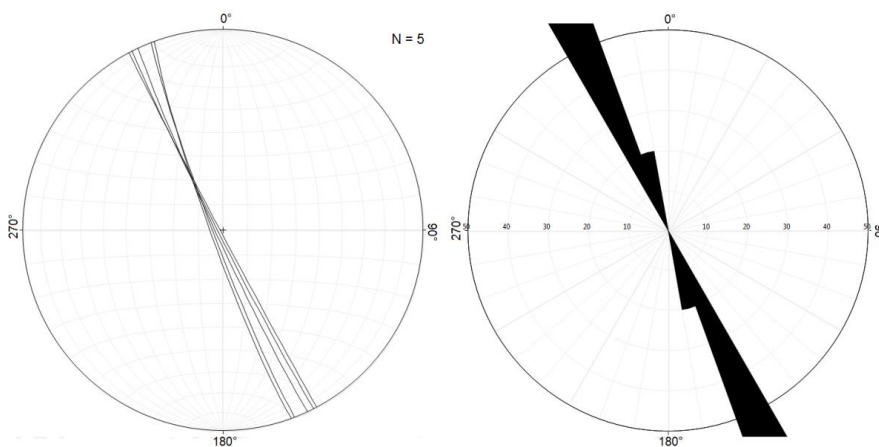
Figura 56. Stereoplot and rose diagram of the second set of joints.

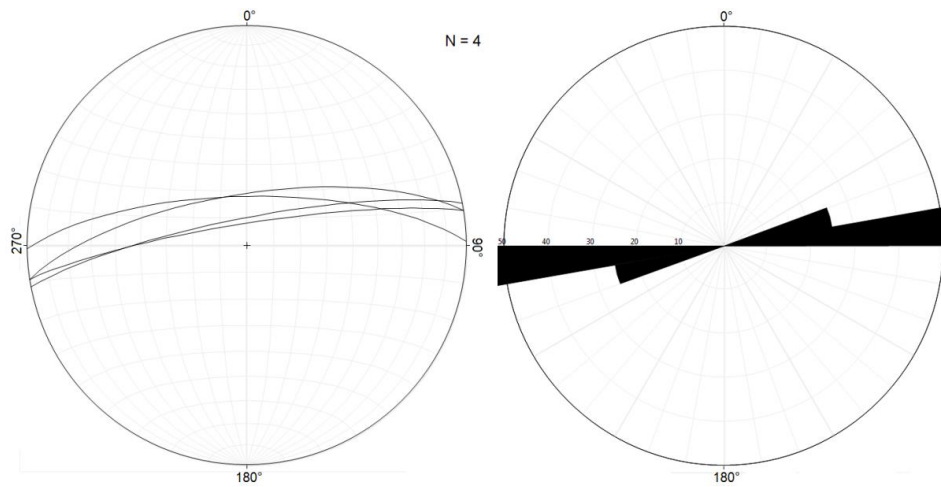Group 3: Facets detected: 4; average strike: N 262°; average dip: 76°.

Group3	dip	dip direction	strike
1	82	351	261
2	80	349	259
3	71	351	261
4	72	359	269

Figure57. Stereoplot and rose diagram of the third set of joints.

The analysis of mesoscale fractures is limited to a descriptive level: the few data collected and the uncertainty caused by the difficulty to orient the point cloud, do not allow carrying out more complete and exhaustive studies.

The comparison of the local scale structural data and those collected at the regional scale in the same area shows that the orientation of the three groups of fracture planes does not match with the two sets found on the Tepui surface.
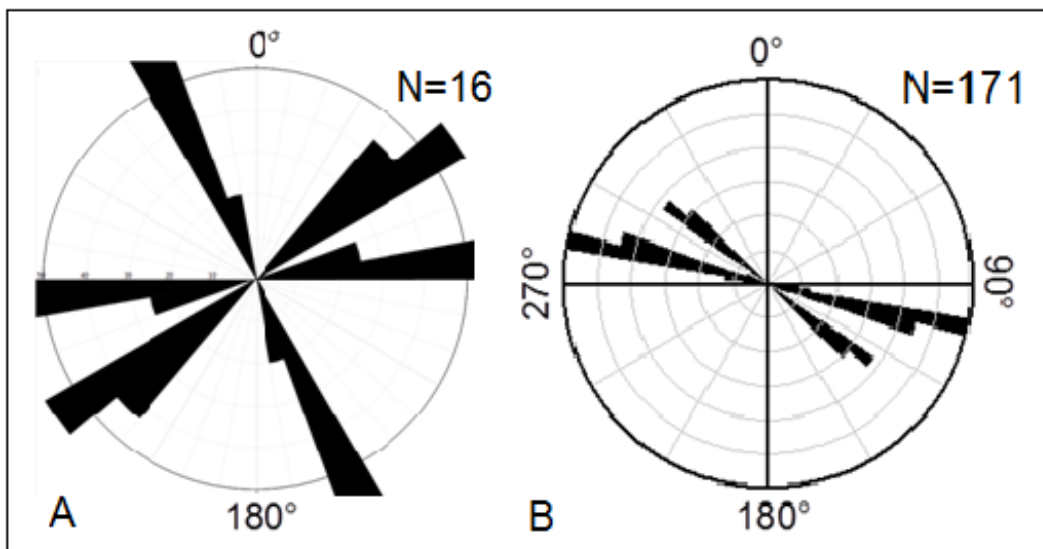
Figure 58. Comparison between A) orientation of the fractures extracted by the point cloud, and B) Orientation of the regional scale fractures in Auyan Tepui.

Looking at a different outcrop, also located at entrance of the cave, we can easily notice that the stack of quartzite strata show an alternation of densely fractured layers and, apparently, massive undeformed banks. The layer characterized by this strata-bounded fracturation shows curious pillar morphologies, which can be referred to the lower resistance to erosion of the fractured strata.

Data collected by Francesco Sauro (2014) from three different station of measurement inside the Imawarì - Yeuta cave, show the presence of nine different strata-bounded fracture sets, with a large range of orientations. Apparently, three of these nine fracture sets correspond with those found from analysis of the point

cloud. At this point, it is hard to determine a genetic relationship between the two different ranks of fractures (regional and meso-scale).

Figure 59. Evidences of alternation between strata-bounded fractured layers and undeformed layers (La Venta - Theraphosa).

According to Brenner and Gudmundsson (2004), strata-bound intense fracturing is typical of alternation of strata with different petrographic and rheological characteristics, which reflects in different Young modulus; these fractures can be also related to regional stresses distributed along strata with different thickness (Pollard and Segall, 1987); According to Sauro (2014), the coexistence of stratabounded joints and more continuous fractures cutting all the strata (and connected vertically to the surface) can be the response of different stress regimes through time.

A further interpretation of the strata-bounded fractures involves the hydrofracturing caused by the fluid overpressure during diagenesis

(Gudmundsson and Brenner, 2001; Brenner and Gudmundsson, 2004; Philipp et al., 2006).
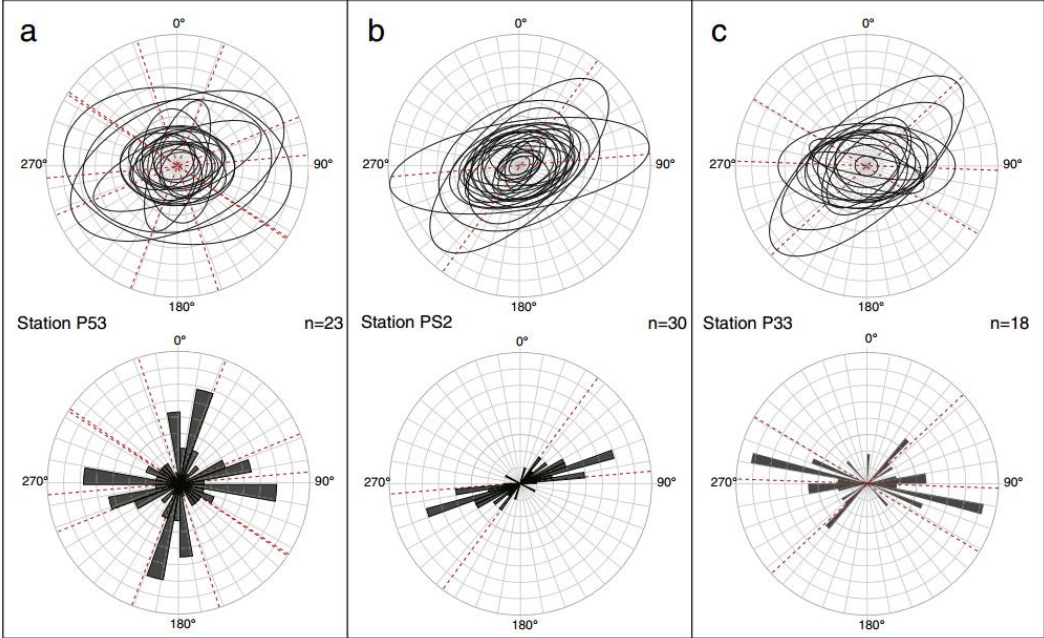
Figure 60. Fracture orientation from three stations of measurements inside the Imawarì Yeuta cave. The petals of the rose diagrams show the main axis of the columnar pillars, while the fracture directions are represented by the red dotted lines (Sauro 2014).

6. Conclusions

The multi-spectral analysis of satellite image has allowed to improve the portion of the Geologic Map of Venezuela regarding my study area; in particular, it has been detected and mapped the presence of argillic alteration, and the boundaries between the various units have been drawn with better accuracy.

The analysis of the fracture systems of the Auyan and Chimantà Tepuis has highlighted the existence of four high angle main joint sets (macro-scale joints) cutting the exposed part of the stratigraphic succession, i.e. the meso-Proterozoic Mataui formation. No offset has been observed along the most prominent fractures, belonging to the N 30° direction. Therefore, the interpretation of that these fractures as true strike-slip faults is ruled out, even if a small horizontal slip, compared to the length of the fractures, cannot be excluded.

The analysis of the geological map of Venezuela reveals the presence of a deformation responsible for gentle folds with NNE-SSW axis, corresponding to the circa N-S axis detected by Briceno (1990). However, the presence of multiple folding events can be inferred from the double-plunging syncline of the Cerro Aradan, west to Auyan Tepui. Therefore, a WNW-ESE axis trend can be inferred from the WNW-ESE strike of the beds well prominent along the southern limit of the tepuis, which locally controls also the rivers flow direction. This second folding event could correspond to the NW-SE axis trend detected by Briceno (1990).

About the relative age of the two folding events, we tentatively suggest that the WNW-ESE axes predate the origin of the NNE-SSW axes, which seem correlated with the origin of the brittle fracture system. In contrast, the first folding could have been originated in a ductile environment, without development of fractures.
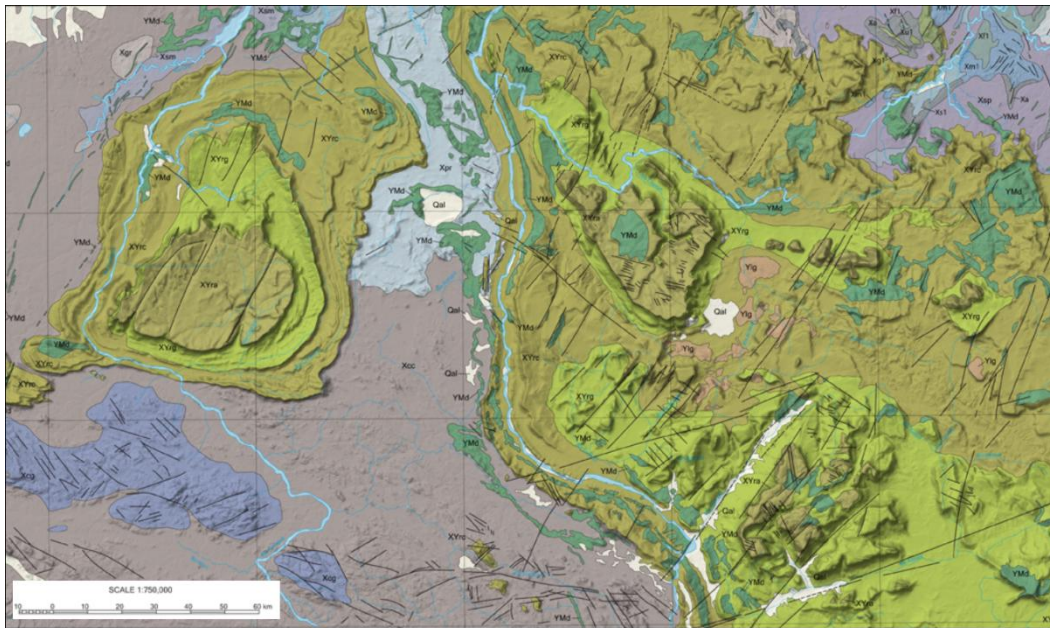
Figure 61. Detail of the geologic map of Venezuela. Three main Tepuis are recognizable: from the west to the east they are the Cerro Aradan, the Auyan Tepui and the Chimantà massif.

The stress field responsible for the second folding event and the related fractures could have been generated in the late Cretaceous by ridge push forces, which took place following the formation of the Mid-Atlantic Ridge and the opening of the south Atlantic Ocean (125 Ma).

Recently, the current intraplate stress fields in South America were inferred from focal mechanisms by Assumpcao et al. (2016): The data, reported on a map (Fig. 61) show that the area of the Guiana Shield is affected by a compressive stress, with NW-SE main principal stress axis (S_{Hmax}) similar to that we found in this thesis.
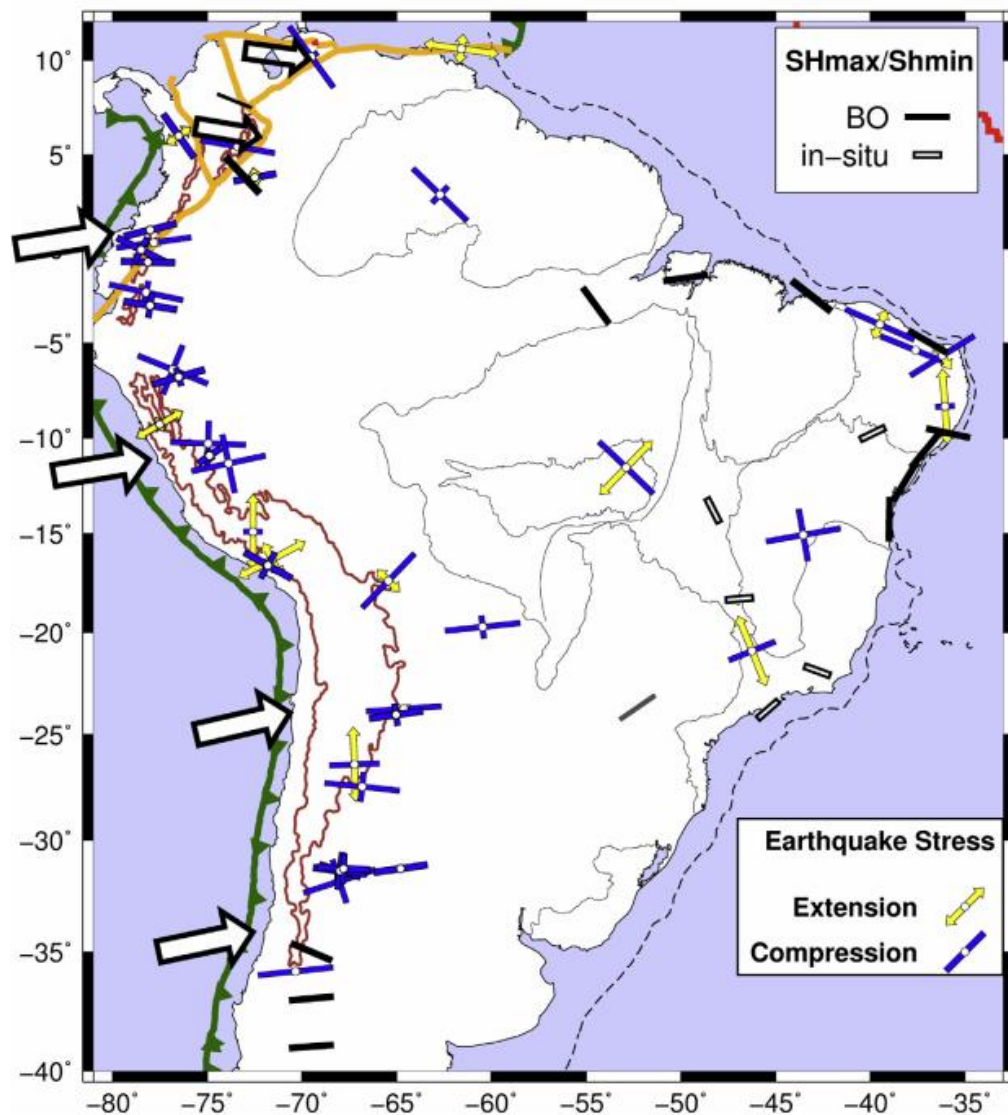
*Figure 62. Distribution of intraplate stresses in South America. (Assumpcao et al., 2016).*

According to various authors (Assumpcao, 1992; Zobach, 1992) the intraplate stresses in South America can be explained by four major sources:

- Ridge-push forces;
- Spreading stresses from lateral density variations in the lithosphere (such as between the Andean plateau and the stable South American platform);

- Plate interaction forces (such as in the Nazca-South America convergent margin);

- Lithosphere/astenosphere basal drag.
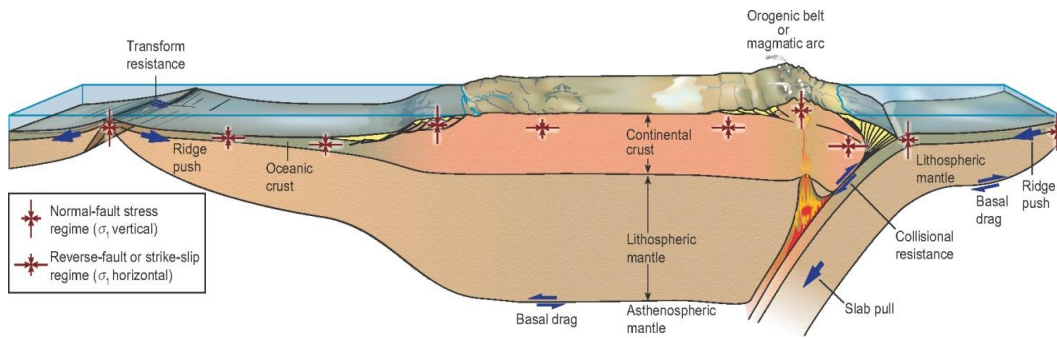
Figure 63. Cross section of the lithosphere, with the forces related to plate tectonic (blue arrows) and stress regimes expected (red arrows). (Fossen, 2000).

Moreover, we can observe that during the spreading between Africa and South America continents, there has been a clockwise rotation of the South American block, until reaching the current position. Accordingly, the horizontal stress axes may have rotated too.
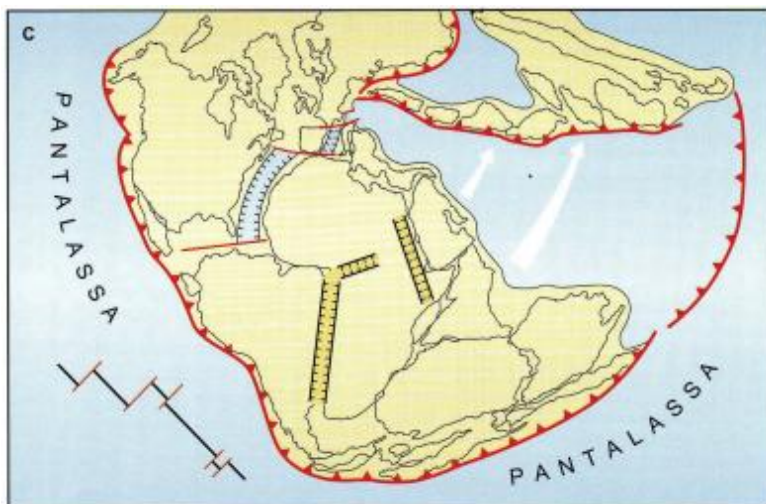

Figure 3. picture of Gondwana continent, before the opening of the South Atlantic Ocean.

Therefore, the prominent fracture system observed in the Tepuis can be related to the last folding event, probably dated to the Late Cretaceous. The orientation of

the main fractures is around N 30°, while two sets of joints are oblique with respect to it and interpreted to as conjugate. On the surface of Chimantà Massif, the bisector of the angle formed by the conjugate joints is N 120°, almost perpendicular to the major fractures direction: in Auyan Tepui, the joints intersect with a slightly narrower angle with respect to that found on Chimantà.
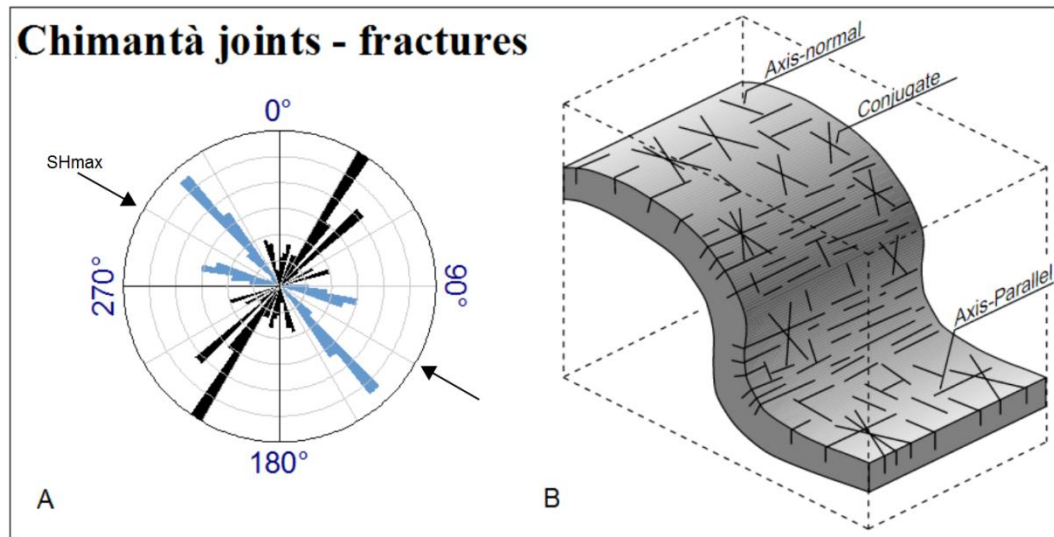
Figure 64. Comparison between: A) the fracture pattern geometry found in the study area, and B) the schematic representation of the fractures associated to folding (Fisher and Wilkinson, 2000, modified from Cooper 1992).

Further examples comes from Cooper (1992): the sketch reported in the Fig. 64 shows an anticline and syncline couple of folds, with development of parallel joints in corrispondence of the hinges, with axis-normal conjugate joints on the sides. Studies carried out by Zampieri (2003) on the Belluno syncline show a similar fracture pattern, with the development of fractures parallel to the fold axis in proximity to the hinge zone, and conjugate sistems of oblique joints in the limbs. Accordingly, in the study area we can infer a main compressive stress oriented NW/SE perpendicular to the fold axes.

The meso-scale fractures observed in the layers affected by the development of the caves and controlling the shape of the pillars connecting the floor and the roof

seem due to different processes, probably related to the diagenesis of the sediment.

References

Allmendinger, R.W., Cardozo, N., and Fisher, D., 2012, *Structural geology algorithms: Vectors and tensors in structural geology*. Cambridge University Press.

Assumpcao M., 1993. The *regional intraplate stress field in South America*. Journal of Geophysical Research 97, 11.889 - 11.903.

Assumpcao M., Dias F. L., Zevallos I., Naliboff J. B., 2016. *Intraplate stress field in South America from earthquake focal mechanisms.* Journal of South American Earth Science 71, 278-295.

Briceno H., C. Shubert, J. Paolini, 1990. *Table-mountain geology and surficial geochemistry: Chimantà Massif, Venezuelan Guayana Shield*. Journal of South American Earth Sciences 3, 179-194.

Brivio A.P., Lechi G., Zilioli E., 2006. *Principi e metodi di telerilevamento*. CittàStudi edizioni.

Cardozo, N., and Allmendinger, R.W., 2013. *Spherical projections with OSXStereonet*. Computers & Geosciences 51, 193 – 205.

Cox D.P., Wynn J.C., Sidder G.B. and Page N.J., 1993. Geology of the Venezuelan Guyana Shield, in Geology and mineral resource assessment of the Venezuelan Guyana Shield. U.S. Geological Survey Bulletin 2062, 9–15.

Cooper M., 1992.*The analysis of fracture systems in subsurface thrust structures from the Foothills of the Canadian Rockie.* in McClay K. R., *Thrust tectonics.* London, Chapman and Hall, 391-405.

Dalton L.V., 1912, *On the geology of Venezuela*: Geological Magazine 9, 203–210.

Dewez, T. J. B., Girardeau-Montaut, D., Allanic, C., and Rohmer, J. *Facets: a cloudcompare plugin to extract geological planes from unstructured 3D point clouds.* Int. Arch. Photogramm. Remote Sens. Spatial Inf. Sci., XLI-B5, 799-804.

Drury S.A., 1987 first edition. *Image interpretation in geology*. Published by Allen and Uniwin.

Fischer M., Wilkerson S.M., 2000. *Predicting the orientation of joints from fold shape: Results of pseudo–three-dimensional modeling and curvature analysis.* Geology 28, 15-18.

Fossen H., 2000 first edition. *Structural Geology.* Cambridge University Press.

Gibbs A.K. and Olszewski W.J., 1982. *Zircon U-Pb ages of Guyana greenstone-gneiss terrane*. Precambrian Research 17, 199–214.

Gonzales de Juana C., J.M. Iturralde de Arozena ad X. Picard, 1980. *Geologia de Venezuela y de sus Cuencas petroliferas*. Ediciones Foninves, Caracas.

Hackey P. C., Urbani F., Karlsen A. W., Garrity C. P., 2005. *Geologic shaded relief map of Venezuela.* United States Geological Survey.

Hirt C., Filmer M. S., Featherstone W. E., 2010. *Comparison and validation of the recent freely-available ASTER-1 GDEM ver 1, SRTM ver 4.1 and GEODATA DEM-9S ver 3 digital elevation models over Australia*. Australian Journal of Earth Science 57, 337-347.

Jenness, J. 2014. *Polar plots for ArcGIS*. Jenness Enterprises. Software available at: http://www.jennessent.com/arcgis/polar_plots.htm.

Lillesand T., Kiefer R. W., Chipman J., 1994. *Remote Sensing and Image Interpretation.* John Wiley & Sons Inc.

Mantovani F., Marcolongo B., 1992. *Fotogeologia. Il telerilevamento nelle scienze della Terra*. Carrocci editore.

Pouyllau M., Seurin M., 1985. *Pseudo-karst clans les roches greso-quartzitiques de la Formation Roraima*. Karstologia 5, 45-52.

Reid A. R., 1974. *Stratigraphy of the type area of the Roraima Group, Venezuela*. Boletin de Geologia (Venezuela), Publicacion Especial 6, 343-352.

Reid A. R. and Bisque R. E., 1975. *Stratigraphy of the diamond-bearing Roraima Group, Estado Bolivar, Venezuela*. Quartarly Bulletin of the Colorado School of Mines 70, 61-82.

Reis N.J., and Yanez G., 2001, *O Supergrupo Roraima ao longo da faixa fronteiric ̧a entre Brasil-Venezuela (Santa Elena del Uairen - Roraima Mountain)*, in Reis, N.J., and Monteiro, M.A.S., eds., Contribuicao a geologia da Amazonia, Volume 2: Manaus, Brazil, Sociedade Brasileira de Geologia, 113–145.

Reis N.J., Pinheiro S.S., Costi H.T., and Costa J.B.S., 1990. *A cobertura sedimentar proterozoica media do Supergrupo Roraima no norte do Estado de Roraima, Brasil: Atribuicoes aos seus sistemas deposicionais eesquema evolutivo da sua borda meridional*, in Anais, Congresso Brasileiro de Geologia, 36th, Natal, Brazil: Sao Paulo, Brazil, Sociedade Brasileira de Geologia,Nucleo Nordeste, 66–81.

Santagata T., Lugli S., Camorani M. E., Ercolani M., 2015. *Laser scanner survey and TRU view applications of the "Grotta della Lucerna", a roman mine for Lapis Specularis.* Hipogea 2015 - proceedings of internetional congress of speleology in artificial cavities.

Santos J.O.S., Hartmann L.A., Gaudette H.E., Groves D.I., Mcnaughton N.J., and Fletcher I.R., 2000. *A new understanding of the provinces of the Amazon Craton based on Integration of Field Mapping and U-Pb and Sm-Nd Geochronology*. Gondwana Research 3, 453-488.

Santos J.O.S., Potter P.E., Reis N.J., Hartmann L.A., Fletcher I.R. and Mcnaughton N.J., 2003. *Age, source, and regional stratigraphy of the Roraima Supergroup and Roraima-like outliers in northern South America based on U-Pb geochronology.* GSA Bulletin 115, 331–34.

Sauro F., 2014. *Structural and lithological guidance on speleogenesis in quartz-sandstone: Evidence of the arenisation process.*Geomorphology 226, 106 - 123.

Sauro F., 2014. *Speleogenesis and secondary cave minerals in quartz-sandstone and quartzite environment.* Tesi di dottorato, Università di Bologna.

Sauro F., Santagata T., Spotl C., De Waele J., 2016. *Amulti-year monitoring project of the high - altitude Cenote ice cave, Dolomiti.*, EGU general Assembly 2016. Geophisical Research Abstracts, vol.18.

Teixeira W., Tassinari C.C.G., Szabo G.J., Mondin M., Sato K., Santos A.P. and Siso C.S., 1999. *Sm-Nd constraints on protolith age of the Archean Imataca Complex.* Venezuela in Actas, South American symposium on isotope geology, 136–138.

Zampieri D., Grandesso P. 2003. *Fracture networks on the Belluno syncline, a fault-propagation fold in the footwall of the Belluno thrust, Venetian Alps, NE Italy.* Geological Society, London, Special Publications 2009, 101-106.

Zoblach M. L., 1992. *First and second order patterns of stress in the lithosphere: the world stress map project.* Journal of Geophysical Research 97, 11.703 - 11.728.

Other resources considered:

- Slide of Remote Sensing course, Matteo Massironi
- landsat.usgs.gov;
- asterweb.jpl.nasa.gov/gdem.asp;
- http://www.esa.int/ESA;

- sentinel.esa.int
- scihub.copernicus.eu

Acknowledgement

First of all, I would like to thank my supervisor, Prof. Dario Zampieri, for the help and support received during all the steps of the realization and writing of this thesis.

I also want to thank Prof. Matteo Massironi, for teaching me the basics of remote sensing and for the accurate correction of some specific chapters.

This thesis would not have been possible without the precious contribute of Prof. Francesco Sauro, to whom I express my gratitude for giving me the opportunity to work on this project, and for the encouragement and the suggestions received.

Many thanks to Tommaso Santagata for the Laser scanner data, and for the help to understand the mechanism of CloudCompare.

Thanks to the photographers of "La Venta Geographic Exploration" Alessio Romeo, Vittorio Crobu, Natalino Russo, Riccardo de Luca and Fulvio Iorio, holders of many pictures used in this work.

And most of all, the greatest thanks goes to my girlfriend Veronica, my brother Enrico and my parents Fabrizio and Gabriella, to my family, my flatmates and to all my friends that always support me.